

國立臺灣大學電機資訊學院電信工程學研究所

博士論文

Graduate Institute of Communication Engineering

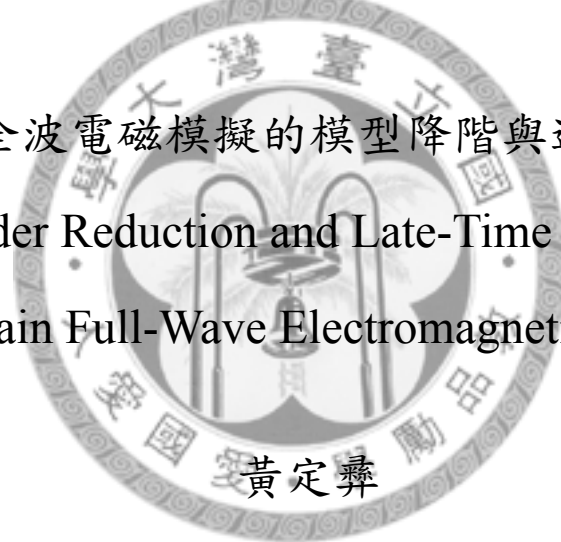
College of Electrical Engineering and Computer Science

National Taiwan University

Doctoral Dissertation

時域全波電磁模擬的模型降階與遲時響應

Model Order Reduction and Late-Time Responses of
Time-Domain Full-Wave Electromagnetic Simulations



Huang, Ting-Yi

指導教授：吳瑞北 博士

Advisor: Wu, Ruey-Beei, Ph.D.

中華民國九十七年七月

July, 2008



摘要

本論文提出於時域電磁全波模擬過程中輔以 Krylov 子空間模型降階的混合型方法，有效率地求得封閉系統的遲時響應。在本論文提出的混合型方法中，模型降階程序通常於激發源消失之後啟動，負責萃取出系統主要且活躍的模態，並利用這些模態的線性組合建構系統的遲時響應。由於有效利用在空間上得到的資訊，在訊源消失並於系統中往返之後，此方法只需要少數額外的時域迭代就能夠得到足夠數量的激發模態。適當地萃取出系統的主要模態之後，便可以輕易地用解析公式重建系統的遲時響應。利用本論文中提出的技巧來實現這類型的混合方法，現存的時域模擬程式碼將得以重覆使用。論文之中亦提供數個數值模擬範例以供檢驗此類方法的正確性、效率、收斂性以及複雜度。由這些範例中皆可以觀察到模型降階程序只需運作少量步驟，混合方法便能得到與直接進行時域計算相當一致的結果。



Abstract

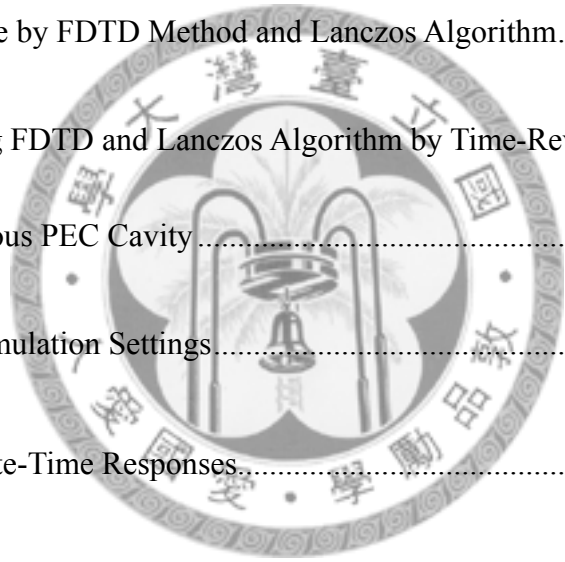
Hybrid methods combining time-domain full-wave electromagnetic simulation and Krylov subspace based model order reduction techniques are proposed for efficiently obtaining the late-time responses of closed systems. In general, model order reduction process is applied after the sources fade to zero for extracting the active modes in the system. Late-time responses are then constructed by the linear combination of the extracted modes. Taking advantage of the space information, only few direct time domain iterations are required after the sources fade to zero with additional round-trip time before the extraction of the excited modes. After the dominant modes are properly extracted, the late time response of the system can be easily reconstructed by analytic expressions. With the proposed hybridizing techniques, existing codes of time-domain simulation can be resorted. Several numerical examples are provided for the verification of the correctness, efficiency, convergence, and complexity of the proposed hybrid methods, which show that with only very few iterations of model order reduction, good agreement can be achieved between the results of the proposed hybrid methods and those obtained from direct time-domain iterations.



Table of Contents

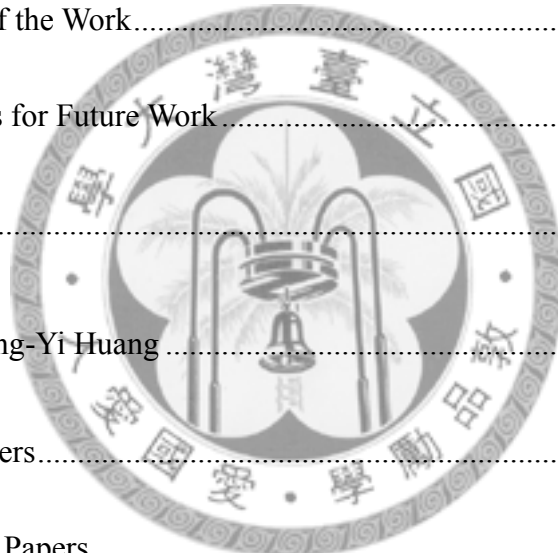
Table of Contents	i
List of Figures	v
1 Introduction.....	1
1.1 Research Motives.....	1
1.2 Literature Survey.....	4
1.3 Contributions	7
1.4 Chapter Outlines	9
2 Theory.....	13
2.1 Finite-Difference Time-Domain Method.....	14
2.1.1 Time Marching in TDTD.....	15
2.1.2 FDTD Equations in Matrix Form	17
2.1.3 Time-Reversal FDTD Equations	19
2.2 Delaunay-Voronoi Modeling of Power-Ground Planes in Time-Domain. 20	
2.2.1 Delaunay-Voronoi Modeling of Power-Ground Planes	23

2.2.2	Time Marching Scheme for Delaunay-Voronoi Modeling of Power-Ground Planes	26
2.3	Model Order Reduction with Krylov Subspace Methods	28
2.3.1	Krylov Subspaces	29
2.3.2	Lanczos Algorithm	30
3	Late-Time Response by FDTD Method and Lanczos Algorithm.....	33
3.1	Hybridizing FDTD and Lanczos Algorithm by Time-Reversal technique.	34
3.2	Homogeneous PEC Cavity.....	42
3.2.1	Simulation Settings.....	42
3.2.2	Late-Time Responses.....	44
3.2.3	Modal Patterns.....	47
3.3	Inhomogeneous PEC Cavity.....	47
3.3.1	Simulation Settings.....	47
3.3.2	Late-Time Responses.....	49
3.3.3	Modal Patterns.....	53



3.4	Convergence and Complexity.....	53
3.4.1	Convergence	54
3.4.2	Complexity.....	56
3.5	Summary of the Chapter	59
4	Late-Time Response for Delaunay-Voronoi Modeling of Power-Ground Planes in Time-Domain with Krylov Subspace Method.....	61
4.1	Krylov Subspace Method for Delaunay-Voronoi Modeling of Power-Ground Planes in Time-Domain.....	62
4.2	Power-Ground Plane of Simple Geometry	68
4.2.1	Geometry	68
4.2.2	Simulation Results	70
4.2.3	Modal Patterns	73
4.3	A More Realistic Power-Ground Plane.....	76
4.3.1	Geometry	76
4.3.2	Simulation Results	79
4.3.3	Modal Patterns	82

4.4	Convergence and Complexity	84
4.4.1	Convergence	84
4.4.2	Complexity	90
4.5	Summary of the Chapter.....	93
5	Conclusions	95
5.1	Summary of the Work.....	96
5.2	Suggestions for Future Work.....	97
References	101
Publication List of Ting-Yi Huang	107
A.	Journal Papers.....	107
B.	Conference Papers.....	109



List of Figures

Fig. 2.1	Yee's cell [1] for discretization of Maxwell equation for the finite-difference time-domain method in three-dimension.	14
Fig. 2.2	A simplified structure for analyzing the problems of power-ground planes with practical source ports [22].	21
Fig. 2.3	Modeling possible paths of current flow between the two practical source ports at high frequencies compared with the electrical dimension by adding virtual ports on the planes [22].	22
Fig. 2.4	Typical setting for the Delaunay-Voronoi modeling of power-ground planes. (a) The arrangement of triangular meshes and the placement virtual ports. (b) The equivalent lumped circuit associated with the practical source port i and the virtual ports connected.	23
Fig. 3.1	Obtaining the matrix-vector product in the Lanczos algorithm without direct computing by the standard FDTD and its time-reversal form. ...	37
Fig. 3.2	Model-order reduction by time-reversal FDTD and Lanczos algorithm	

applying to (3.2a). (a) Block diagram for the direct computing loop of (3.2a). (b) Block diagram for the model-order reduction loop with $\mathbf{q}_1 = \mathbf{E}^{n_0}$ 40

Fig. 3.3. The flow chart of the hybrid method proposed in this chapter, where the matrix-vector product of the Lanczos algorithm is accomplished by standard and time-reversal FDTD, as shown in Fig. 3.2.41

Fig. 3.4 An air-filled PEC cavity of dimension 10 cm by 10 cm by 1 cm.....43

Fig. 3.5. The late-time responses of the z-component of the electric field at point A obtained by brute-force FDTD and the hybrid method with different numbers of modes extracted.44

Fig. 3.6. The late-time responses of the z-component of the electric field at points B and C obtained by brute-force FDTD and the hybrid method with two modes extracted.45

Fig. 3.7. Modal patterns of the first two modes extracted by Lanczos algorithm. (a) The first mode extracted; (b) the second mode extracted.46

Fig. 3.8. An air-filled PEC cavity with a dielectric object.....48

Fig. 3.9.	The late-time responses of (a) the y-component at the point (0.5 , 10 , 10)(mm) and (b) the x-component at the point (15 , 0.5 , 10)(mm) of the magnetic field in Fig. 3.5 which is excited by a Gaussian pulse with a longer rise time.....	50
Fig. 3.10.	The late-time responses of the y-component of the magnetic field at the point (0.5 mm, 10 mm, 10 mm) in Fig. 4 which is excited by a Gaussian pulse with a shorter rise time.	51
Fig. 3.9.	Modal patterns of the magnetic field at the $z = 10\text{mm}$ plane in the structure shown in Fig. 3.8 for the first six modes extracted by Lanczos algorithm.....	52
Fig. 3.12.	The absolute value of the smallest expansion coefficient a_{\min} normalized to the largest one, a_{\max} , which is obtained at each of the Lanczos iteration in the second example described in the previous section.	55
Fig. 3.13.	The magnitude of the frequency response of the magnetic field obtained at the point (0.5 mm, 10 mm, 10 mm) in Fig. 4 in the second example in IV with a high frequency excitation.....	58

Fig. 4.1.	Constructing a Krylov subspace for the approximation of system matrix \mathbf{A} directly from a series of system response in time.....	63
Fig. 4.2.	Flow chart of the hybrid method proposed in this chapter, where the Krylov subspace is constructed directly from the pre-stored voltage vectors as shown in Fig. 4.1.	66
Fig. 4.3.	The geometry of a 50mm×50mm×1.6mm power-ground plane with an excitation port at (20mm, 30mm). (a) Three-dimensional view. (b) Top view.....	69
Fig. 4.4.	Mesh setting for the simulation of the structure shown in Fig. 4.3. (a) Locations of the input port (solid dot) and virtual ports (double circle). (b) Arrangement of the triangular meshes on the plane.....	70
Fig. 4.5.	Late-time responses obtained by direct time-domain iteration (solid line) and hybrid method (dashed line) for the structure with a geometry shown in Fig. 4.3 and a mesh settings in Fig. 4.4.....	71
Fig. 4.6.	The frequency responses of the input impedance at the port of Fig. 4.3 obtained by direct inverting the Y-matrix in frequency domain (solid	

line) and the frequency transform by FFT of the late-time responses obtained by direct time-domain iteration (dashed line) and the hybrid method (dotted line)..... 72

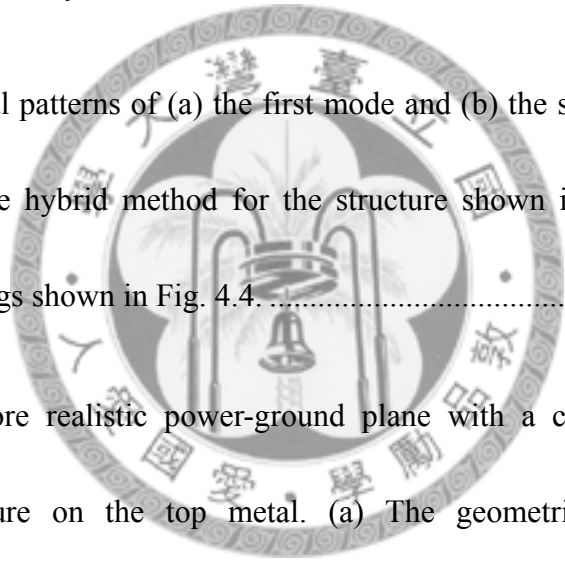
Fig. 4.7 Frequency responses and modal patterns obtained by (4.9) for the cavity shown in Fig. 4.3 with (a) $m=1, n=0$ (b) $m=0, n=1$, and (c) $m=1, n=1$, respectively. 74

Fig. 4.8. Modal patterns of (a) the first mode and (b) the second mode extracted by the hybrid method for the structure shown in Fig. 4.3 with mesh settings shown in Fig. 4.4. 75

Fig. 4.9. A more realistic power-ground plane with a clipped corner and an aperture on the top metal. (a) The geometric parameters of the power-ground plane. (b) The mesh setting for simulation..... 77

Fig. 4.10. (a) The time response of a standard Gaussian pulse and (b) its frequency response; and (c) the time response of a modulated Gaussian pulse with zero DC level and (d) its frequency response. 78

Fig. 4.11. The magnitude of the frequency responses of the input impedance at the



port shown in Fig. 4.9. The solid line is obtained by direct inverting the Y-matrix in frequency domain. The dashed and dash-dotted lines are the results by time-domain iteration and FFT with two different sources of excitation.80

Fig. 4.12. The magnitude of the frequency responses of the input impedance at the port shown in Fig. 4.9 obtained by direct time-domain iteration (solid line) and the hybrid method (dashed line) with FFT.81

Fig. 4.13. (a) The first mode and (b) the second mode of the structure shown in Fig. 4.9, which are extracted by the hybrid method; and (c) the first mode and (b) the second mode of the same structure extracted by Ansoft® HFSS™.83

Fig. 4.14. (a) Mesh1, a coarse mesh setting, (b) Mesh2, a marginal mesh setting, and (c) Mesh3, a fine mesh setting arranged for the verification of self convergence of the hybrid method proposed in this chapter.87

Fig. 4.15. Frequency responses of the input impedances at the incident port denoted by black dots in Fig 4.13 for mesh settings Mesh1 (dotted line), Mesh 2 (dashed line), and Mesh3 (solid line).88

Fig. 4.16. Modal patterns extracted by the hybrid method. (a) The first mode and (b) the second mode extracted from Mesh1; and (c) The first mode and (d) the second mode extracted from Mesh2..... 89





1

Introduction

TIME-domain full-wave electromagnetic simulations have been widely used in modern digital and analog circuit design. This thesis proposes a model-order reduction technique for the late-time responses of time-domain full-wave electromagnetic simulation. As an introduction, the research motives of this work will be discussed first in this chapter. Literature survey of related works is then presented, followed by the major contribution of this work. Outlines of each chapter will also be briefly described in the end of this chapter.

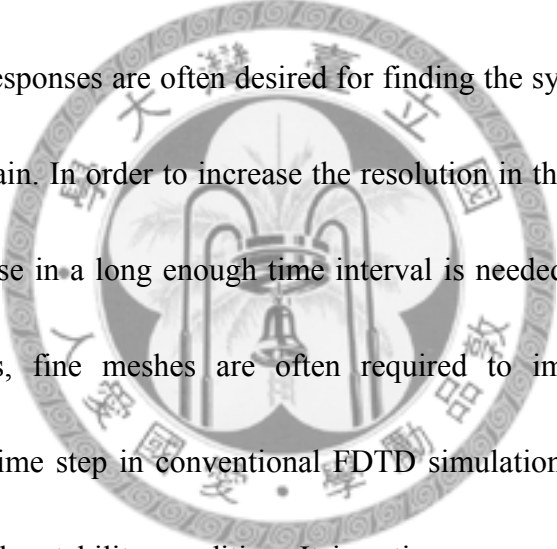
1.1 Research Motives

Modern electronic circuits are often composed of digital and analog hybridization. As the fabrication processes such as very large scale integrated (VLSI) circuit and low-temperature co-fire ceramic (LTCC) advance, the complexity and

circuit size has grown to an extraordinary level. Operation speed and frequency range of the signal also increases rapidly as computer and communication applications mature. Circuit level simulation no longer satisfies the precision desire for some critical parts or even the whole circuits at design stage. On the other hand, full-wave electromagnetic simulation provides accurate results with the expenses of time and memory requirement of computation. Typical design procedure has then become extracting the characteristics such as scattering coefficients or impedance matrices of the critical parts, and then the extracted “black boxes” become new circuit components in the circuit level simulation. Therefore time-domain full-wave methods are often preferred in package level co-simulation, especially when dealing with cases where non-linear components are presented, due to their easy integration with existing commercial circuit simulation software packages, e.g. SPICE.

The finite-difference time-domain (FDTD) method [1], [2] is well known for its simple implementation and high efficiency in solving various general-purpose problems. In general, sources such as Gaussian pulses or time-domain reflectometry (TDR) signals are injected into the areas of interest and a few field points wherein are often chosen to be observed. The FDTD solvers update all the field points in the

areas continually as time marching until the injected energies decay to a certain level. The relation between observing field points and injecting sources are then set up to find the characteristics such as transfer functions or scattering parameters of the system. However, this strategy fails in most low-loss close problems and some open problems with high-Q materials. The energies decay very slowly or may even remain at a nonconverging level permanently in certain cases.



Steady-state responses are often desired for finding the system characteristics in the frequency domain. In order to increase the resolution in the frequency domain, a steady-state response in a long enough time interval is needed to be calculated. For complex structures, fine meshes are often required to improve accuracy and, consequently, the time step in conventional FDTD simulation should also be small enough to satisfy the stability condition. It is a time-consuming task to obtain the frequency-domain characteristics under such conditions. In addition, only a few field points need to be taken into consideration in most practical applications while fields at all points in the computational domain should be calculated at each time iteration. How to efficiently get the steady-state response at those field points concerned therefore becomes an important subject. [3]

1.2 Literature Survey

Techniques commonly used for the extrapolation of late-time responses in FDTD simulations are Prony's methods [2], [4]-[8]. It is a technique for modeling sampled data as a linear combination of complex exponentials, therefore particularly suitable for calculating the resonant frequency and Q of a resonating structure [2]. With data sampled at a relatively small number of time iterations, the late-time responses can be effectively predicted [6]. However, temporal data are needed to be sampled at a sufficient number of locations, or the frequency-domain circuit parameters will not be accurate [8].

Another way to retrieve the spectral-domain data from timedomain simulators are the filter-diagonalization methods [2], [9]-[13]. This technique recasts the problem of spectral analysis of a short segment of a time-dependent signal into an eigenvalue problem [2]. These methods are useful in extracting the mode frequencies and decay constants of high- Q cavities [12]. With properly chosen basis sets, the spectral parameters obtained by the filter-diagonalization method can be used to construct a high resolution Fourier spectrum, circumventing the Fourier uncertainty

principle [13]. Therefore, cases of nearly degenerate modes can be effectively handled.

The aforementioned techniques usually deal with data sampled in a long period of time at few points. Increasing the sample temporal points can improve the accuracy, but with larger computational overhead as a tradeoff. On the other hand, it can be advantageous to exploit the space information that is necessary to be updated at each FDTD iteration. Model-order reduction techniques combining with the FDTD that recently arose are the Lanczos algorithms [14], [15]. Taking advantages of the sparsity of the equivalent matrix of the FDTD operator, although still large in size, the model order can be efficiently reduced since the Lanczos algorithm is able to convert a large sparse matrix into a much smaller tridiagonal matrix with very low overheads. The eigenvalues of the reduced matrix are approximately equal to some of the extremal eigenvalues of the original matrix. The associated eigenvectors of the original matrix can also be recovered from the eigenvectors of the reduced matrix through a simple transformation.

Several papers have been proposed for dealing with the model-order reduction of the FDTD method by the Lanczos algorithm. A modified Lanczos algorithm is

proposed for the computation of transient electromagnetic fields [16]. Accurate representation of the transient electromagnetic fields is obtained on a certain bounded interval in time. However, this is not suitable for obtaining the steady-state response for practical problems since more Lanczos iterations may be required in order to increase the time interval of accurate simulation. Tradeoffs between divergence owing to loss of orthogonality and slow convergence due to re-orthonormalization will arise as Lanczos iterations increase [15].

Rapid FDTD simulation without time stepping is also proposed [17]. With the reduced-order model extracted by the Lanczos algorithm, the response can be obtained at any frequency. However, the number of FDTD update equations is doubled. The original system and its adjoint problem are both needed because the asymmetric Lanczos algorithm is applied [18].

This work provides a different approach in combining the FDTD method and Lanczos algorithm based on [19]. The basic theory is detailed in Chapter 2 and the hybrid method as well as some numerical examples are provided in Chapter 3. With the Lanczos algorithm, modes for a source-free FDTD operator concerning either electric or magnetic fields only are extracted. Utilizing the time-reversal property of

the FDTD [20], the existing FDTD codes can be resorted to directly.

For the analysis of power-ground plane issues in high-speed digital circuit systems, an efficient model of power-ground planes based on the concept of model network has been proposed [21], [22]. A novel model consisting of the virtual ports and triangular meshes with the distributed lumped circuit elements is established, which has the advantages of constructing the SPICE-compatible models to facilitate the multi-layer design analysis for power-ground planes. With little modifications, a time marching scheme similar to FDTD based on this method can be combined with Krylov subspace methods

1.3 Contributions

As mentioned in the previous section, this work provides a novel approach combining the FDTD method and Lanczos algorithm. Unlike other approaches which take time information over few space samples into consideration, the proposed hybrid method utilizes the space information which is automatically evaluated every time step in FDTD. Since the most time consuming bottleneck is FDTD iteration itself, less iterations needed for completing a model order reduction process is

preferred.

Taking advantages of the space information, Lanczos algorithm extracts dominant modes rapidly. This means only few FDTD iterations are needed for the proposed hybrid method to converge. The modal information is then used to construct the late-time response of the system. Only the responses at those points concerned is computed with nearly constant order of complexity. After introducing time-reversal FDTD into the hybrid method, with little modification, existing FDTD code are also preserved.

Another hybrid method dealing with time-domain model order reduction for analyzing the power-ground planes of high-speed digital circuit systems is also proposed in this thesis. Based on the efficient model of power-ground planes presented in [22], a time marching scheme similar to FDTD is constructed. Krylov subspace method is then applied to extract the dominant mode according to the space information computed at each time step. After the modal information has been extracted, the late-time responses of the system at those points concerned are also easily determined with nearly constant order of complexity.

Unlike the FDTD/Lanczos hybrid method, time-reversal scheme is not available

for the time-domain method utilized in this hybrid method. The Krylov subspace is instead constructed from a series of space information which are stored at different time steps. With additional memory overhead, the existing codes of the time-domain method can also be preserved.

Several examples are provided for both hybrid methods, ranging from simple demonstration cases to more realistic applications. In addition to the presented simulation results for the examples, the convergence and complexity for both methods are further discussed also with a few simulation results to verify the robustness and effectiveness of the proposed methods.

1.4 Chapter Outlines

In order to provide a systematic and structured presentation of this work, the remaining contents of the thesis are organized as follows.

The basic theory which both hybrid methods based on will be described in Chapter 2. A brief review of the finite-difference time-domain method will be presented firstly, including the traditional iterative FDTD equations and its matrix form, equations involving both the electric and magnetic fields, as well as those with

single field only. Time-reversal technique for FDTD will also be described. The time-domain method based on Delaunay-Voronoi modeling of power-ground planes will then be discussed, which shows how a time marching scheme similar to FDTD can be established from the efficient power-ground plane model. The last part of chapter 2 shows the key component of both hybrid methods, i.e., model order reduction with Krylov subspace methods. With these methods modes of systems can be extracted effectively for the reconstruction of late-time responses.

Chapter 3 presents the first hybrid method which efficiently evaluates the late-time response by combining finite-difference time-domain method and Lanczos algorithm. Technique that hybridizing FDTD and Lanczos Algorithm by introducing time-reversal FDTD equations is firstly described, followed by numerical examples with a homogeneous PEC cavity and an inhomogeneous PEC cavity with different excitations. Convergence and complexity is then discussed with verification from the simulation results.

The other hybrid method that reconstructs the late-time response for Delaunay-Voronoi modeling of power-ground planes in time-domain with Krylov subspace method is presented in Chapter 4. After describing the hybridizing

technique that applies Krylov subspace method on the Delaunay-Voronoi modeling of power-ground planes in time-domain, several examples inclusive of power-ground planes of a simple geometry and a more realistic power-ground plane is demonstrated. The convergence and complexity for this method is also analyzed and verified with simulation results.

The thesis is then concluded with a summary of this work. A few suggestions for the future works will also be provided.





2

Theory

THE hybrid methods presented in this work is based on the basic theory described in this chapter. The finite-difference time-domain (FDTD) method will be briefly reviewed first. The traditional iterative FDTD equations and its matrix form, equations involving both the electric and magnetic fields and those with single field only, and time-reversal technique for FDTD will be described. Based on the Delaunay-Voronoi modeling of power-ground planes provided in [22], a time marching scheme similar to FDTD is developed. The key component of the proposed hybrid methods, model order reduction with Krylov subspace methods, with which the modes of a system are extracted effectively for the reconstruction of late-time responses, will be discussed in the last part of this chapter.

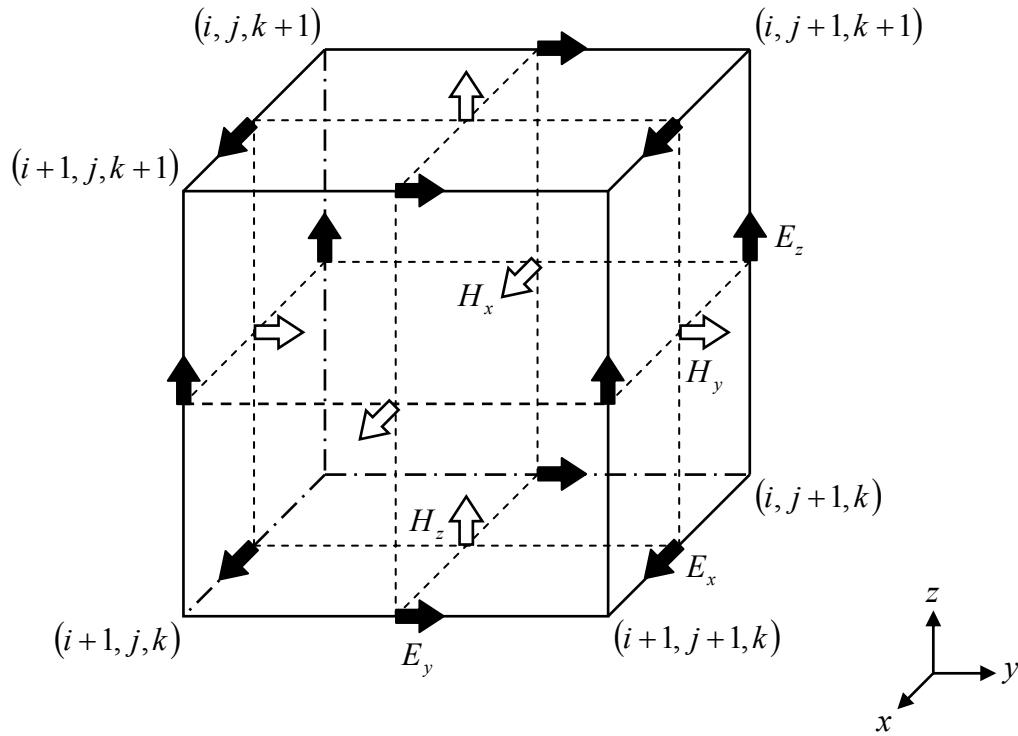


Fig. 2.1 Yee's cell [1] for discretization of Maxwell equation for the finite-difference time-domain method in three-dimension.

2.1 Finite-Difference Time-Domain Method

The derivation of finite-difference time-domain equations in source free regions begins with source free Maxwell equations.

$$\nabla \times \vec{E} = -\frac{\partial \vec{B}}{\partial t} \quad (2.1a)$$

$$\nabla \times \vec{H} = \frac{\partial \vec{D}}{\partial t} \quad (2.1b)$$

2.1.1 Time Marching in TDTD

In source-free region with lossless isotropic media, (2.1) can be discretized with the Yee's cell [1] setting shown in Fig. 2.1, where the simplified coordinate notation (i, j, k) denotes the point located at $(i\Delta x, j\Delta y, k\Delta z)$, integer multiples i, j , and k of the space discretization $\Delta x, \Delta y$, and Δz , respectively. If the discretization in time is denoted as Δt with integer multiples n , the field values of the x -component of the electric field locate at $\left(i + \frac{1}{2}, j, k\right)$ and time step n can be denoted as $E_x|_{i+\frac{1}{2}, j, k}^n$, the field values of the y -component of the magnetic field locate at $\left(i + \frac{1}{2}, j, k + \frac{1}{2}\right)$ and time step $n + \frac{1}{2}$ can be denoted as $H_y|_{i+\frac{1}{2}, j, k}^{n+\frac{1}{2}}$. Notations of other field values can be defined in a similar manner. Applying central difference method for both the differentiation in time and space, the iterative finite-difference time-domain equations can be derived as

$$\eta_0 H_x|_{i, j+\frac{1}{2}, k+\frac{1}{2}}^{n+\frac{1}{2}} = \eta_0 H_x|_{i, j+\frac{1}{2}, k+\frac{1}{2}}^{n-\frac{1}{2}} - \frac{(c \cdot \Delta t)}{\mu_r|_{i, j+\frac{1}{2}, k+\frac{1}{2}}} \left[\frac{E_z|_{i, j+1, k+\frac{1}{2}}^n - E_z|_{i, j, k+\frac{1}{2}}^n}{\Delta y} - \frac{E_y|_{i, j+\frac{1}{2}, k+1}^n - E_y|_{i, j+\frac{1}{2}, k}^n}{\Delta z} \right] \quad (2.2a1)$$

$$\eta_0 H_y \Big|_{i+\frac{1}{2},j,k+\frac{1}{2}}^{n+\frac{1}{2}} = \eta_0 H_y \Big|_{i+\frac{1}{2},j,k+\frac{1}{2}}^{n-\frac{1}{2}} - \frac{(c \cdot \Delta t)}{\mu_r \Big|_{i+\frac{1}{2},j,k+\frac{1}{2}}} \left[\frac{E_x \Big|_{i+\frac{1}{2},j,k+1}^n - E_z \Big|_{i+\frac{1}{2},j,k}^n}{\Delta z} - \frac{E_y \Big|_{i+1,j,k+\frac{1}{2}}^n - E_y \Big|_{i,j,k+\frac{1}{2}}^n}{\Delta x} \right] \quad (2.2a2)$$

$$\eta_0 H_z \Big|_{i+\frac{1}{2},j+\frac{1}{2},k}^{n+\frac{1}{2}} = \eta_0 H_z \Big|_{i+\frac{1}{2},j+\frac{1}{2},k}^{n-\frac{1}{2}} - \frac{(c \cdot \Delta t)}{\mu_r \Big|_{i+\frac{1}{2},j+\frac{1}{2},k}} \left[\frac{E_y \Big|_{i+1,j+\frac{1}{2},k}^n - E_y \Big|_{i,j+\frac{1}{2},k}^n}{\Delta x} - \frac{E_x \Big|_{i+\frac{1}{2},j+1,k}^n - E_x \Big|_{i+\frac{1}{2},j,k}^n}{\Delta y} \right] \quad (2.2a3)$$

$$E_x \Big|_{i+\frac{1}{2},j,k}^{n+1} = E_x \Big|_{i+\frac{1}{2},j,k}^n - \frac{(c \cdot \Delta t)}{\varepsilon_r \Big|_{i+\frac{1}{2},j,k}} \left[\frac{\eta_0 H_z \Big|_{i+\frac{1}{2},j+\frac{1}{2},k}^{n+\frac{1}{2}} - \eta_0 H_z \Big|_{i+\frac{1}{2},j-\frac{1}{2},k}^{n+\frac{1}{2}}}{\Delta y} - \frac{\eta_0 H_y \Big|_{i+\frac{1}{2},j,k+\frac{1}{2}}^{n+\frac{1}{2}} - \eta_0 H_y \Big|_{i+\frac{1}{2},j,k-\frac{1}{2}}^{n+\frac{1}{2}}}{\Delta z} \right] \quad (2.2b1)$$

$$E_y \Big|_{i,j+\frac{1}{2},k}^{n+1} = E_y \Big|_{i,j+\frac{1}{2},k}^n - \frac{(c \cdot \Delta t)}{\varepsilon_r \Big|_{i,j+\frac{1}{2},k}} \left[\frac{\eta_0 H_x \Big|_{i,j+\frac{1}{2},k+\frac{1}{2}}^{n+\frac{1}{2}} - \eta_0 H_x \Big|_{i,j+\frac{1}{2},k-\frac{1}{2}}^{n+\frac{1}{2}}}{\Delta z} - \frac{\eta_0 H_z \Big|_{i+\frac{1}{2},j+\frac{1}{2},k}^{n+\frac{1}{2}} - \eta_0 H_z \Big|_{i-\frac{1}{2},j+\frac{1}{2},k}^{n+\frac{1}{2}}}{\Delta x} \right] \quad (2.2b2)$$

$$E_z \Big|_{i,j,k+\frac{1}{2}}^{n+1} = E_z \Big|_{i,j,k+\frac{1}{2}}^n - \frac{(c \cdot \Delta t)}{\varepsilon_r \Big|_{i,j,k+\frac{1}{2}}} \left[\frac{\eta_0 H_y \Big|_{i+\frac{1}{2},j,k+\frac{1}{2}}^{n+\frac{1}{2}} - \eta_0 H_y \Big|_{i-\frac{1}{2},j,k+\frac{1}{2}}^{n+\frac{1}{2}}}{\Delta x} - \frac{\eta_0 H_x \Big|_{i,j+\frac{1}{2},k+\frac{1}{2}}^{n+\frac{1}{2}} - \eta_0 H_x \Big|_{i,j-\frac{1}{2},k+\frac{1}{2}}^{n+\frac{1}{2}}}{\Delta y} \right] \quad (2.2b3)$$

, where $\eta_0 = \sqrt{\frac{\mu_0}{\varepsilon_0}}$ is the intrinsic impedance of free space and c is the velocity of

light in free space. At time step n , the magnetic field is first updated to the next half time step by (2.2a) with the electric field at current time step and magnetic field at previous half time step; the updated magnetic field at next half time step and the electric field at current time step is used to update the electric field to the next time step by (2.2b). After updating both fields, the FDTD iteration in a time step is completed. Time step is then moved from n to $n+1$. Repeatedly, the desired time responses of both fields can be evaluated.

2.1.2 FDTD Equations in Matrix Form

Let \mathbf{E}^n and \mathbf{H}^n be the column vectors formed by the electric and magnetic field values at time step n in (2.2), respectively. The FDTD update equation can be cast into matrix form as

$$\eta_0 \mathbf{H}^{n+\frac{1}{2}} = \eta_0 \mathbf{H}^{n-\frac{1}{2}} - (\mathbf{c} \cdot \Delta t) \cdot \boldsymbol{\mu}_r^{-1} \cdot \mathbf{D} \cdot \mathbf{E}^n \quad (2.3a)$$

and

$$\mathbf{E}^{n+1} = \mathbf{E}^n + (\mathbf{c} \cdot \Delta t) \cdot \boldsymbol{\epsilon}_r^{-1} \cdot \mathbf{D}^T \cdot \eta_0 \mathbf{H}^{n+\frac{1}{2}}, \quad (2.3b)$$

where \mathbf{D} denotes the discrete curl operator. Substitute (2.3a) and the $(n-1)$ -th time step of (2.3b) into the n -th time step of (2.3b), the FDTD update equation in matrix

form can be written as

$$\begin{bmatrix} \eta_0 \mathbf{H}^{n+\frac{1}{2}} \\ \mathbf{E}^{n+1} \end{bmatrix} = \begin{bmatrix} \mathbf{I} & -(c \cdot \Delta t) \cdot \boldsymbol{\mu}_r^{-1} \cdot \mathbf{D} \\ (c \cdot \Delta t) \cdot \boldsymbol{\epsilon}_r^{-1} \cdot \mathbf{D}^T & \mathbf{I} - (c \cdot \Delta t)^2 \cdot \boldsymbol{\epsilon}_r^{-1} \cdot \mathbf{D}^T \cdot \boldsymbol{\mu}_r^{-1} \cdot \mathbf{D} \end{bmatrix} \begin{bmatrix} \eta_0 \mathbf{H}^{n-\frac{1}{2}} \\ \mathbf{E}^n \end{bmatrix}, \quad (2.4)$$

where the identity matrix is denoted by \mathbf{I} .

Eliminating the equations involving magnetic fields in (2.4) yields an update equation with electric field only.

$$\mathbf{E}^{n+1} = 2 \cdot \left[\mathbf{I} - \frac{1}{2} (c \cdot \Delta t)^2 \cdot \boldsymbol{\epsilon}_r^{-1} \cdot \mathbf{D}^T \cdot \boldsymbol{\mu}_r^{-1} \cdot \mathbf{D} \right] \cdot \mathbf{E}^n - \mathbf{E}^{n-1} \quad (2.5a)$$

On the other hand, an update equation with only magnetic field concerned can also be obtained.

$$\eta_0 \mathbf{H}^{n+\frac{1}{2}} = 2 \cdot \left[\mathbf{I} - \frac{1}{2} (c \cdot \Delta t)^2 \cdot \boldsymbol{\mu}_r^{-1} \cdot \mathbf{D} \cdot \boldsymbol{\epsilon}_r^{-1} \cdot \mathbf{D}^T \right] \cdot \eta_0 \mathbf{H}^{n-\frac{1}{2}} - \eta_0 \mathbf{H}^{n-\frac{3}{2}}. \quad (2.5b)$$

These two matrix equations with only a single field in (2.5) play an important role in the next chapter, where Lanczos algorithm is applied to the symmetric matrix inside the bracket. With the hybridizing technique which will be detailed later, direct evaluation of (2.5) is not required. Existing code of FDTD solvers can be reused with the introducing of additional time-reversal FDTD equations.

2.1.3 Time-Reversal FDTD Equations

The time-reversal technique in FDTD method has been proposed for the numerical synthesis of a microwave structure [20]. By slightly rearranging (2.3), the update equation can be operated backward in time as

$$\eta_0 \mathbf{H}^{n-\frac{1}{2}} = \eta_0 \mathbf{H}^{n+\frac{1}{2}} + c \cdot \Delta t \cdot \boldsymbol{\mu}_r^{-1} \cdot \mathbf{D} \cdot \mathbf{E}^n \quad (2.6a)$$

and

$$\mathbf{E}^{n-1} = \mathbf{E}^n - c \cdot \Delta t \cdot \boldsymbol{\epsilon}_r^{-1} \cdot \mathbf{D}^T \cdot \eta_0 \mathbf{H}^{n-\frac{1}{2}}. \quad (2.6b)$$

The time-reversal FDTD iterations proceed in a similar manner as ordinate FDTD. At time step n , the magnetic field is first updated to the previous half time step by (2.6a) with the electric field at current time step and magnetic field at next half time step; the updated magnetic field at previous half time step and the electric field at current time step is then used to update the electric field to the previous time step by (2.6b). After updating both fields, another iteration begins with the time step moving from n to $n-1$.

For the hybrid method presented in the following chapter, the time-reversal FDTD equations will only activate after the model order reduction procedure begins.

As long as the model order reduction procedure converges rapidly, the computation overhead increased by introducing the time-reversal FDTD equation and the numerical error cumulates in the backward iteration in time [20] can be minimized.

2.2 Delaunay-Voronoi Modeling of Power-Ground Planes in Time-Domain

A simplified structure is shown in Fig. 2.2 for analyzing the problems of power-ground planes with practical source ports [22]. A pair of close-spaced power-ground planes with length l and width w are separated by a dielectric substrate with a thickness h and a relative dielectric constant ϵ_r . Two source ports, port A and port B , are placed in the plane for the modeling of via structures through the planes. Current injecting into port A may induce a power-ground bounce noise between the planes. The noise wave travels throughout the entire planes and eventually the noise will couple to port B , causing a slightly variation to the port voltage.

Fig. 2.3 shows the modeling of possible paths of current flow between the two practical source ports at high frequencies compared with the electrical dimension by adding virtual ports on the planes [22]. As the wavelength of interests approaches the

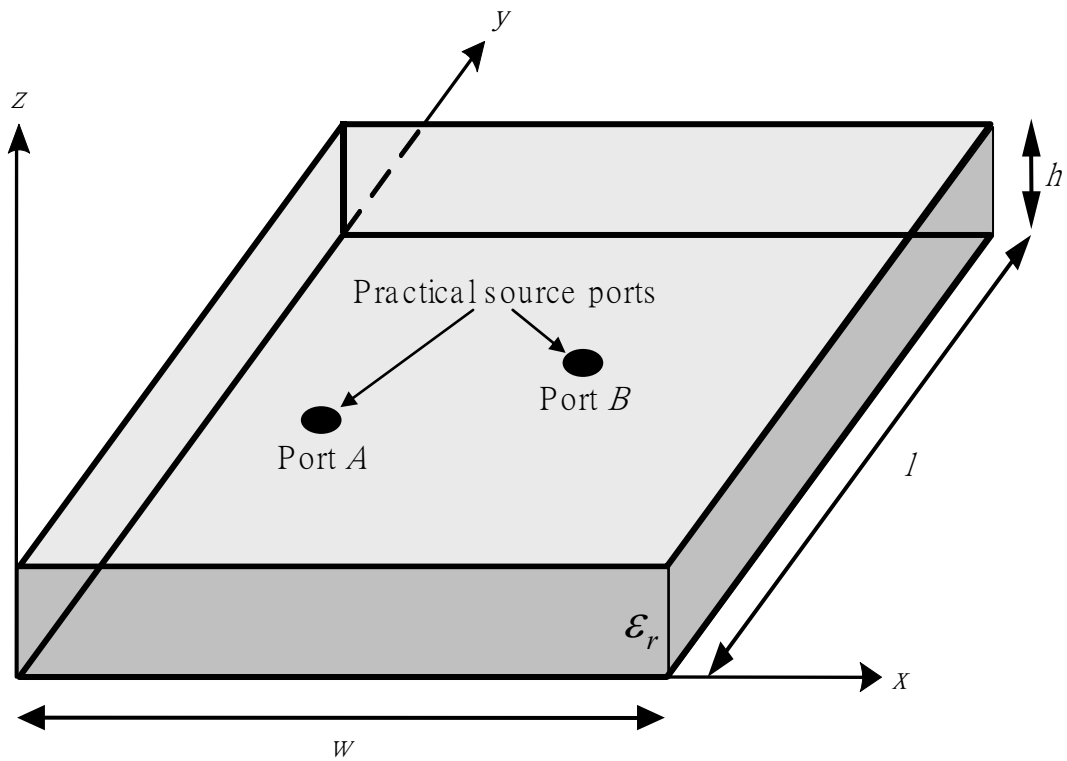


Fig. 2.2 A simplified structure for analyzing the problems of power-ground planes with practical source ports [22].

electrical dimensions of the interconnection structures, the current does not flow straightly from port *A* to port *B* but also includes the paths spreading radially outward from port *A* and then reflecting from the edges of power-ground planes to port *B*. This phenomenon can be effectively modeled by the novel method proposed in [22] using an equivalent lumped circuit model with virtual ports that play the role of the distributed current transition. The values of lumped circuit elements are associated

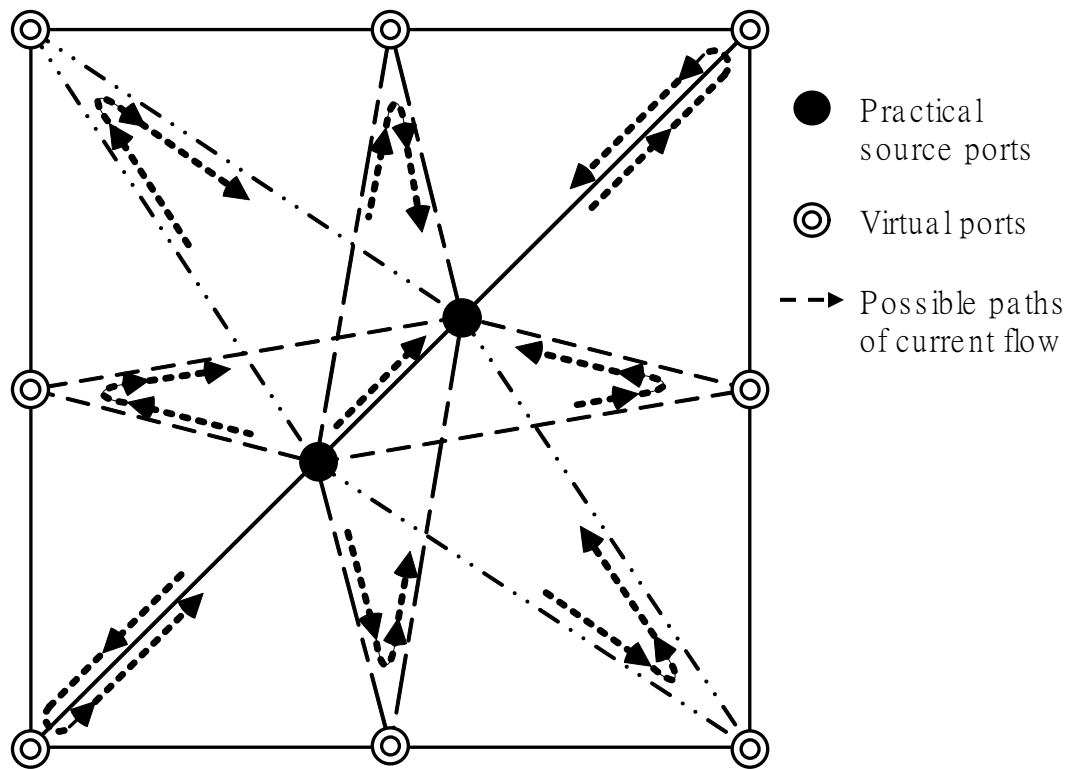


Fig. 2.3 Modeling possible paths of current flow between the two practical source ports at high frequencies compared with the electrical dimension by adding virtual ports on the planes [22].

with the geometry of the triangular mesh and can be obtained by employing the Delaunay triangularization for the mesh generation and applying Voronoi tessellation at each node.

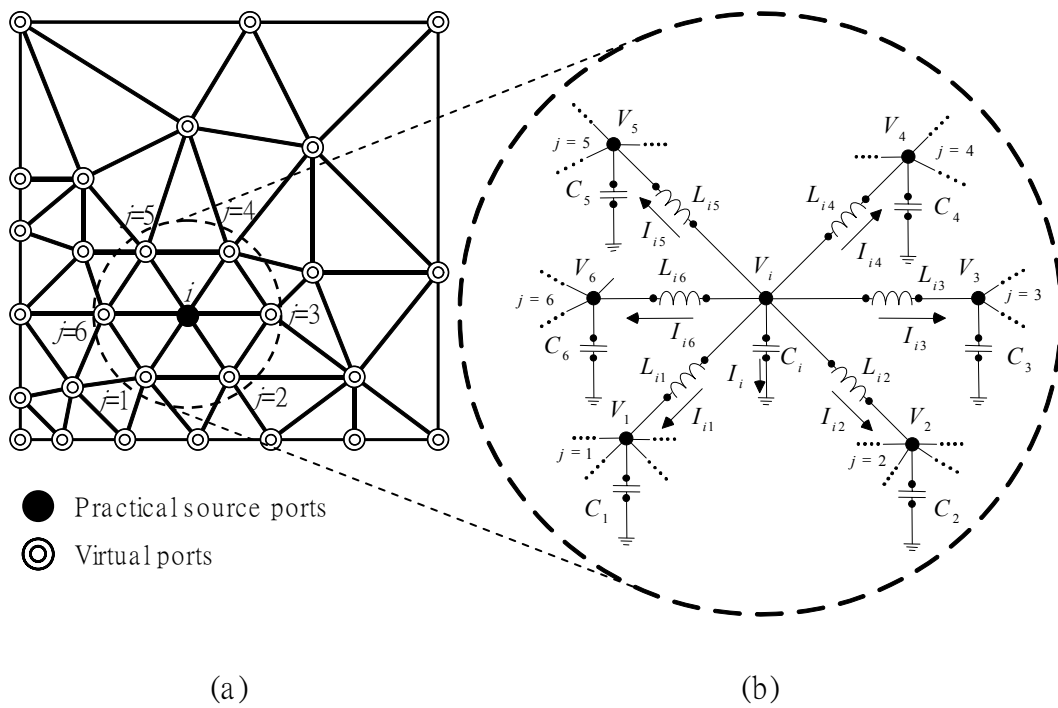


Fig. 2.4 Typical setting for the Delaunay-Voronoi modeling of power-ground planes. (a) The arrangement of triangular meshes and the placement virtual ports. (b) The equivalent lumped circuit associated with the practical source port i and the virtual ports connected.

2.2.1 Delaunay-Voronoi Modeling of Power-Ground Planes

For the typical setting of Delaunay-Voronoi modeling of power-ground planes shown in Fig. 2.4, if the arrangement of triangular meshes and the placement virtual

ports is given in Fig. 2.4a, the equivalent lumped circuit associated with the practical source port i and its connecting neighbor virtual ports, which are embraced in the dashed circle, can be determined as Fig. 2.4b, assume a lossless condition. The values of the elements in the equivalent lumped circuit model can be determined by matching the terms derived from the perspective of circuit and electromagnetic theory.

Applying the Kirchhoff's Current Law (KCL), the relation between nodal voltages and the lumped circuit elements at the i -th node in Fig. 2.4 can be obtained as



$$j\omega C_i V_i + \sum_{j=1}^6 \frac{V_i - V_j}{j\omega L_{ij}} = 0 \quad (2.7)$$

with the notations shown in Fig. 2.4b, where the nodal voltages at the i - and j -th node are denoted by V_i and V_j , respectively. The shunt capacitance at the i -th node is denoted by C_i and L_{ij} represents the series inductance connecting the i - and j -th node.

On the other hand, if the thickness h in Fig. 2.2 is small enough compare to the wavelength of interest, the voltage distribution can be approximate as a function of

coordinates (x, y) , the electric and magnetic field can be written as

$$\vec{E} = -\frac{V(x, y)}{h} \hat{z} \quad (2.8a)$$

and

$$\vec{H} = \frac{1}{j\omega\mu h} (\nabla V(x, y) \times \hat{z}), \quad (2.8b)$$

respectively. Applying Ampere's Law $\oint \vec{H} \cdot d\vec{l} = I + \iint j\omega\epsilon \vec{E} \cdot d\vec{s}$ to the i -th node in Fig. 2.4, with integration along the path connecting the circumcenters of the triangular mesh surrounding the node, the integral on both sides of the equation can be derived as

$$\oint \vec{H} \cdot d\vec{l} = \sum_{j=1}^6 \frac{V_i - V_j}{j\omega\mu h d_{ji}} l_{ji} \quad (2.9a)$$

and

$$\iint j\omega\epsilon \vec{E} \cdot d\vec{s} = j\omega\epsilon \frac{V_i}{h} A_i, \quad (2.9b)$$

where d_{ji} is the length of the line connecting the j - and i -th node, l_{ji} is the length between the circumcenters of the two triangles with a common edge connecting the j - and i -th node, and A_i is the area of the integration loop. Detailed derivation can be found in [22].

By matching the terms in (2.7) and (2.9), the values of the lumped circuit elements is then determined as

$$C_i = \varepsilon \frac{A_i}{h} \quad (2.10a)$$

and

$$L_{ij} = \frac{\mu h d_{ij}}{l_{ij}}, \quad (2.10b)$$

which shows a relation only with the geometric parameters. Therefore once the meshes for the analysis are set, these values can then be uniquely defined.

2.2.2 Time Marching Scheme for Delaunay-Voronoi Modeling of Power-Ground Planes

For the i -th node of the equivalent lumped circuit model of power-ground planes shown in Fig. 2.4b, the node voltage and the branch current can be related with the lumped circuit elements in time domain as

$$I_i = C_i \frac{dV_i}{dt} \quad (2.11a)$$

and

$$V_i - V_j = L_{ij} \frac{dI_{ij}}{dt}, \quad (2.11b)$$

where V_i and V_j is the node voltage at the i - and j -th node, respectively, I_i is the current through the shunt capacitance C_i , and I_{ij} is the current through the series inductance L_{ij} connecting the i - and j -th node. These two current can be related by KCL as

$$I_i + \sum_j I_{ij} = 0. \quad (2.11c)$$

Since the current flows from the i - to j -th node in the opposite direction as from j - to i -th node, it is obvious that $I_{ij} = -I_{ji}$ when (2.11) is applied to the j -th node.

Let the time in (2.11) be discretized as $n \cdot \Delta t$. If the node voltages is located at the integer multiples as $V_i^n = V_i(n \cdot \Delta t)$ and the branch current is located at the center of every two contiguous integer multiples as $I_i^{n+\frac{1}{2}} = I_i\left(\left(n + \frac{1}{2}\right) \cdot \Delta t\right)$ and $I_{ij}^{n+\frac{1}{2}} = I_{ij}\left(\left(n + \frac{1}{2}\right) \cdot \Delta t\right)$, applying central difference to the differentiation in time in

(2.11)yields

$$V_i^{n+1} = V_i^n + \frac{\Delta t}{C_i} I_i^{n+\frac{1}{2}} \quad (2.12a)$$

and

$$I_{ij}^{n+\frac{1}{2}} = I_{ij}^{n-\frac{1}{2}} + \frac{\Delta t}{L_{ij}} (V_i^n - V_j^n). \quad (2.12b)$$

(2.11c) can also be rewritten as

$$I_i^{n+\frac{1}{2}} = -\sum_j I_{ij}^{n+\frac{1}{2}} \quad (2.12c)$$

with branch currents $I_{ij}^{n+\frac{1}{2}} = -I_{ji}^{n+\frac{1}{2}}$. For the time marching scheme of Delaunay-Voronoi modeling of power-ground planes, the iteration at time step n begins with (2.12b), where the branch currents through the series inductances connecting the nodes are updated to the next half time step with those at previous half time step and the voltages at all nodes at current time step. The current through the shunt capacitance at each node can then be updated by (2.12c). After that all node voltages can be updated to the next time step with their value at current time step and the currents at next half time step. Time step is then moved from n to $n+1$ for the beginning of a new iteration.

2.3 Model Order Reduction with Krylov Subspace Methods

Model order reduction for linear systems is often associated with a few numbers

of the largest and/or smallest eigenvalues and their eigenvectors. For a large sparse symmetric $n \times n$ matrix \mathbf{A} , the approximation of its extremal eigenvalues can be efficiently extracted through a sequence of tridiagonal matrices generated by Krylov subspace methods, where the extremal eigenvalues of the tridiagonal matrices are progressively better estimates of \mathbf{A} 's extremal eigenvalues [15].

2.3.1 Krylov Subspaces

For a Rayleigh quotient defined as

$$r(x) = \frac{x^T \mathbf{A} x}{x^T x} \quad x \neq 0, \quad (2.13)$$

where \mathbf{A} is a symmetric $n \times n$ matrix and x is a column vector with dimension n , the maximum and minimum values of $r(x)$ can be proved to be the largest and smallest eigenvalues of \mathbf{A} , i.e., $\lambda_1(\mathbf{A})$ and $\lambda_n(\mathbf{A})$, respectively [15].

Define a sequence of orthonormal vectors $\mathbf{Q}_k = [q_1 \quad q_2 \quad \dots \quad q_k]$ and scalars

M_k as

$$M_k = \lambda_1(\mathbf{Q}_k^T \mathbf{A} \mathbf{Q}_k) = \max_{y \neq 0} \frac{y^T (\mathbf{Q}_k^T \mathbf{A} \mathbf{Q}_k) y}{y^T y} = \max_{\|y\|_2=1} r(\mathbf{Q}_k y) \leq \lambda_1(\mathbf{A}), \quad (2.14)$$

and let $u_k \in \text{span}\{q_1, q_2, \dots, q_k\}$ be the vector that $M_k = r(u_k)$, to ensure that

$M_{k+1} > M_k$, q_{k+1} can be selected such that $\nabla r(u_k) \in \text{span}\{q_1, q_2, \dots, q_{k+1}\}$

since $r(x)$ increases the most rapidly in the direction of its gradient

$$\nabla r(x) = \frac{2}{x^T x} (\mathbf{A}x - r(x)x). \quad (2.15)$$

One can easily find that $\nabla r(x) \in \text{span}\{x, \mathbf{A}x\}$, therefore the above problem is equivalent to the computation of orthonormal bases for the k -th order Krylov subspaces

$$\kappa^k(\mathbf{A}, q_1) = \text{span}\{q_1, \mathbf{A}q_1, \dots, \mathbf{A}^{k-1}q_1\}. \quad (2.16)$$

2.3.2 Lanczos Algorithm

For any $n \times n$ symmetric matrix \mathbf{A} and an arbitrary starting vector \mathbf{b} , Lanczos algorithm is able to establish a Krylov subspace of order m [15],

$$\kappa^m(\mathbf{A}, \mathbf{b}) \equiv \text{span}\{\mathbf{b}, \mathbf{A}\mathbf{b}, \dots, \mathbf{A}^{m-1}\mathbf{b}\} = \text{span}\{\mathbf{q}_1, \mathbf{q}_2, \dots, \mathbf{q}_m\}, \quad (2.17)$$

at the m -th iteration by generating an $m \times m$ symmetric tridiagonal matrix \mathbf{T}_m and an $n \times m$ transformation matrix \mathbf{Q}_m , where the columns of \mathbf{Q}_m which form an orthonormal set are called Lanczos vectors. Let α_i and β_i be the i -th element on the diagonal and subdiagonal of \mathbf{T}_m , respectively, i.e.,

$$T_m = \begin{bmatrix} \alpha_1 & \beta_1 & \cdots & 0 \\ \beta_1 & \alpha_2 & & \vdots \\ & & \ddots & \ddots \\ \vdots & & \ddots & \ddots & \beta_{m-1} \\ 0 & \cdots & & \beta_{m-1} & \alpha_m \end{bmatrix}, \quad (2.18)$$

and \mathbf{q}_i be the i -th column of \mathbf{Q}_m . By equating columns in $\mathbf{A}\mathbf{Q}_m = \mathbf{Q}_m\mathbf{T}_m$, i.e.,

$$\mathbf{A} \cdot \mathbf{q}_i = \beta_{i-1} \mathbf{q}_{i-1} + \alpha_i \mathbf{q}_i + \beta_i \mathbf{q}_{i+1}, \quad (2.19)$$

and exploiting the orthonormality of \mathbf{q}_i , the Lanczos iteration can be determined as follows.

Starting with vector \mathbf{b} ,

$$1) \quad \mathbf{r}_0 = \mathbf{q}_1 = \mathbf{b}/\|\mathbf{b}\|, \quad \mathbf{q}_0 = \mathbf{0}, \quad \beta_0 = 1, \quad k = 0.$$

Repeat the following steps until β_k has reached an acceptable tolerance level.

$$2) \quad k := k + 1.$$

$$3) \quad \alpha_k = \mathbf{q}_k^T \cdot \mathbf{A} \cdot \mathbf{q}_k.$$

$$4) \quad \mathbf{r}_k = \mathbf{A} \cdot \mathbf{q}_k - \alpha_k \mathbf{q}_k - \beta_{k-1} \mathbf{q}_{k-1}.$$

$$5) \quad \beta_k = \|\mathbf{r}_k\|.$$

$$6) \quad \mathbf{q}_{k+1} = \mathbf{r}_k / \beta_k.$$

The matrices \mathbf{T}_m and \mathbf{Q}_m obtained in the Lanczos algorithm are then used to approximate the eigenpairs of the original systems. If λ_i^m and $\boldsymbol{\theta}_i^m$ are one of the eigenpairs of \mathbf{T}_m , then an approximate eigenpair of \mathbf{A} , denoted by $\tilde{\lambda}_i$ and $\tilde{\boldsymbol{\theta}}_i$, can be found via the following relations.

$$\tilde{\lambda}_i = \lambda_i^m \quad \text{and} \quad \tilde{\boldsymbol{\theta}}_i = \mathbf{Q}_m \cdot \boldsymbol{\theta}_i^m. \quad (2.20)$$



3

Late-Time Response by FDTD Method and Lanczos Algorithm

A hybrid method combining finite-difference time-domain (FDTD) method and Lanczos algorithm is proposed in this chapter for efficiently obtaining the steady-state response for closed systems. The theory begins with the FDTD equations in isotropic media. Although Lanczos algorithm for asymmetric systems is available theoretically, the symmetric form which is more stable and insensitive to numerical error is preferred here.

A symmetric updating matrix appears in the FDTD equations which only either electric or magnetic fields are involved. Lanczos algorithm is applied to one of the symmetric updating matrices after the sources fade to zero. However, modification of existing FDTD codes is not preferred and can be avoided with the aid of time-reversal FDTD techniques.

The detailed derivation of the hybrid method is described in the first section, followed by numerical examples with a homogeneous PEC cavity and an inhomogeneous PEC cavity with different excitations. Convergence and complexity is then discussed with verification from the simulation results.

3.1 Hybridizing FDTD and Lanczos Algorithm by Time-Reversal technique

As mentioned in 2.1, in isotropic media with relative permittivity $\epsilon_r(\mathbf{r})$ and permeability $\mu_r(\mathbf{r})$, (2.4) shows the source-free Maxwell equation for FDTD method in matrix form, which is rewritten here as

$$\begin{bmatrix} \eta_0 \mathbf{H}^{n+1/2} \\ \mathbf{E}^{n+1} \end{bmatrix} = \begin{bmatrix} \mathbf{I} & -c \cdot \Delta t \cdot \boldsymbol{\mu}_r^{-1} \cdot \mathbf{D} \\ c \cdot \Delta t \cdot \boldsymbol{\epsilon}_r^{-1} \cdot \mathbf{D}^T & \mathbf{I} - (c \cdot \Delta t)^2 \cdot \boldsymbol{\epsilon}_r^{-1} \cdot \mathbf{D}^T \cdot \boldsymbol{\mu}_r^{-1} \cdot \mathbf{D} \end{bmatrix} \begin{bmatrix} \eta_0 \mathbf{H}^{n-1/2} \\ \mathbf{E}^n \end{bmatrix}, \quad (3.1)$$

where \mathbf{I} is the identity matrix, \mathbf{D} denotes the discretized curl operator, Δt is the time step, c denotes the velocity of light in free space, and the superscript n means the n -th time step of FDTD iteration.

The equivalent matrix of FDTD operator in (3.1) is large and sparse, but not symmetric. As (2.5), eliminating either the magnetic or electric field in (3.1) yields

$$\mathbf{E}^{n+1} = 2 \cdot \left[\mathbf{I} - \frac{1}{2} (c \cdot \Delta t)^2 \cdot \boldsymbol{\epsilon}_r^{-1} \cdot \mathbf{D}^T \cdot \boldsymbol{\mu}_r^{-1} \cdot \mathbf{D} \right] \cdot \mathbf{E}^n - \mathbf{E}^{n-1} \quad (3.2a)$$

and

$$\eta_0 \mathbf{H}^{n+1/2} = 2 \cdot \left[\mathbf{I} - \frac{1}{2} (c \cdot \Delta t)^2 \cdot \boldsymbol{\mu}_r^{-1} \cdot \mathbf{D}^T \cdot \boldsymbol{\epsilon}_r^{-1} \cdot \mathbf{D} \right] \cdot \eta_0 \mathbf{H}^{n-1/2} - \eta_0 \mathbf{H}^{n-3/2}. \quad (3.2b)$$

It is obvious that if either the relative permittivity or permeability matrix is homogeneous, one of the updating matrices inside the bracket in (3.2) will be symmetric.

For the common usage of FDTD solvers, e.g., applications at microwave and millimeter-wave frequency or in high-speed digital systems, materials are usually non-magnetic. In other words, $\boldsymbol{\mu}_r$ is an identity matrix in common applications and therefore (3.2b) is usually applicable for obtaining a symmetric updating matrix.

The symmetric updating matrix in (3.2) is theoretically equivalent to the updating matrix in [23], and therefore has eigenvalues of magnitudes no larger than unity. The field vector \mathbf{E}^n or \mathbf{H}^n in (2) can be expanded in terms of the eigenvectors of the updating matrix. If the expansion coefficient corresponding to the j -th eigenvector at n -th time step in the FDTD iterations is denoted by $a_{n,j}$, the following recurrence relation can be obtained by substitution of the expansion

coefficients to (3.2),

$$a_{n+1,j} - 2\lambda_j a_{n,j} + a_{n-1,j} = 0, \quad (3.3)$$

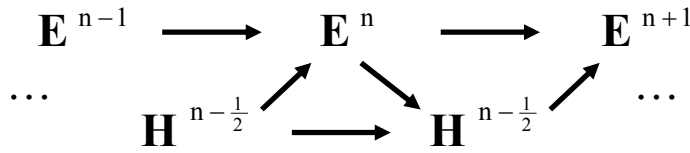
where λ_j is the corresponding j -th eigenvalue of the updating matrix in (3.2).

The second order difference equation in (3.3) can be solved analytically if λ_j and two initial conditions, $a_{n_0,j}$ and $a_{n_0-1,j}$ are given for some time step n_0 . Once (3.3) is solved, the expansion coefficient $a_{n,j}$ at any time step $n \geq n_0 - 1$ can be calculated directly. This can be done for the most significant m -th eigenvectors. Then an approximate solution for the steady-state response of the original large system can be obtained analytically.

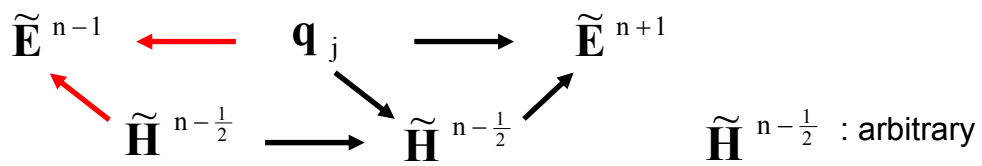
After the electromagnetic sources fade to zero, the modal patterns begin to appear. Lanczos algorithm is then applied to obtain the approximated eigensolutions of the updating matrix in (3.2). The initial \mathbf{b} vector for Lanczos algorithm is set to be the field vector \mathbf{E}^{n_0} or \mathbf{H}^{n_0} in (2) at some time step n_0 , and the \mathbf{A} matrix is chosen to be the corresponding updating matrix.

As described in 2.3.2, the most time consuming part in each Lanczos iteration is the matrix-vector product $\mathbf{A} \cdot \mathbf{q}_k$. Getting these vectors for Lanczos algorithm

Standard FDTD

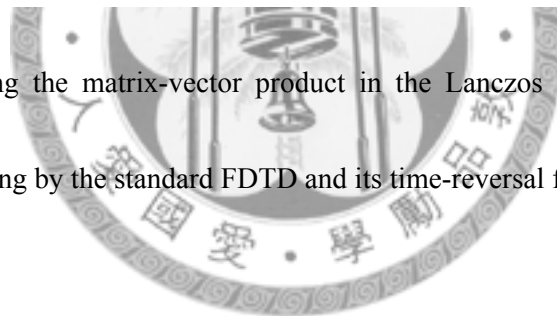


Time-Reversal FDTD



$$\Rightarrow 2 \cdot \mathbf{A} \cdot \mathbf{q}_j = \tilde{\mathbf{E}}^{n+1} + \tilde{\mathbf{E}}^{n-1}$$

Fig. 3.1 Obtaining the matrix-vector product in the Lanczos algorithm without direct computing by the standard FDTD and its time-reversal form.



directly by (3.2) is not preferred because existing FDTD codes cannot be employed directly. Instead, as implied by (3.2), the time-consuming matrix-vector product $\mathbf{A} \cdot \mathbf{q}_k$ can be obtained in a much easier way.

Fig. 3.1 shows how to obtain the matrix-vector product in the Lanczos algorithm without direct computing by the standard FDTD and its time-reversal form.

Assume that Lanczos algorithm is applied to the updating matrix in (3.2a). After k Lanczos iterations the k -th Lanczos vector \mathbf{q}_k can be obtained. Let $\tilde{\mathbf{E}}^n = \mathbf{q}_k$ be the virtual electric field at current time step and $\tilde{\mathbf{H}}^{n-1/2}$ be the virtual magnetic field at half a time step before, the virtual electric field at the previous time step can be obtained by (2.6b),

$$\tilde{\mathbf{E}}^{n-1} = \tilde{\mathbf{E}}^n - c \cdot \Delta t \cdot \boldsymbol{\epsilon}_r^{-1} \cdot \mathbf{D}^T \cdot \eta_0 \tilde{\mathbf{H}}^{n-1/2}, \quad (3.4)$$

and the virtual electric field at the next time step can be obtained from standard FDTD iterations

$$\begin{aligned} \tilde{\mathbf{E}}^{n+1} &= \tilde{\mathbf{E}}^n + c \cdot \Delta t \cdot \boldsymbol{\epsilon}_r^{-1} \cdot \mathbf{D}^T \cdot \eta_0 \tilde{\mathbf{H}}^{n+1/2} \\ &= \tilde{\mathbf{E}}^n + c \cdot \Delta t \cdot \boldsymbol{\epsilon}_r^{-1} \cdot \mathbf{D}^T \cdot \left(\eta_0 \tilde{\mathbf{H}}^{n-1/2} - c \cdot \Delta t \cdot \boldsymbol{\mu}_r^{-1} \cdot \mathbf{D} \cdot \tilde{\mathbf{E}}^n \right). \end{aligned} \quad (3.5)$$

Once $\tilde{\mathbf{E}}^{n-1}$ and $\tilde{\mathbf{E}}^{n+1}$ are determined, $\mathbf{A} \cdot \mathbf{q}_k$ can be easily obtained by reorganizing (3.2a), i.e.,

$$\mathbf{A} \cdot \mathbf{q}_k = \mathbf{A} \cdot \tilde{\mathbf{E}}^n = \frac{1}{2} (\tilde{\mathbf{E}}^{n-1} + \tilde{\mathbf{E}}^{n+1}). \quad (3.6)$$

Also note that the terms associated with virtual magnetic field $\tilde{\mathbf{H}}^{n-1/2}$ are canceled when averaging the virtual electric fields at the previous and next time steps, thus

$\tilde{\mathbf{H}}^{n-1/2}$ is considered as a dummy field vector and can be arbitrary chosen.

The enforcement of boundary conditions can be applied directly for close systems. However, for open problems, the absorbing walls become “injection walls” in time-reversal FDTD simulations [20]. It is therefore necessary to know the time evolution of the field injected from the boundary, which is unknown for the “virtual field” in the Lanczos iterations. The extension of time-reversal FDTD requires further study and is not included here.

The block diagram of the aforementioned procedures is shown in Fig. 3.2 where the model-order reduction procedure by time-reversal FDTD and Lanczos algorithm in Fig. 3.2b is used instead of the direct computing loop in Fig. 3.2a. The overall flow chat of the hybrid is shown in Fig. 3.3. These are summarized as the following steps for clarity. This hybrid method can be repeated in the same manner if Lanczos algorithm is applied to the updating matrix in (3.2b) instead.

- 1) Perform the standard FDTD iterations until all sources fade to zero at time step n_0 .
- 2) Begin Lanczos iterations with starting vector $\mathbf{b} = \mathbf{E}^{n_0}$.

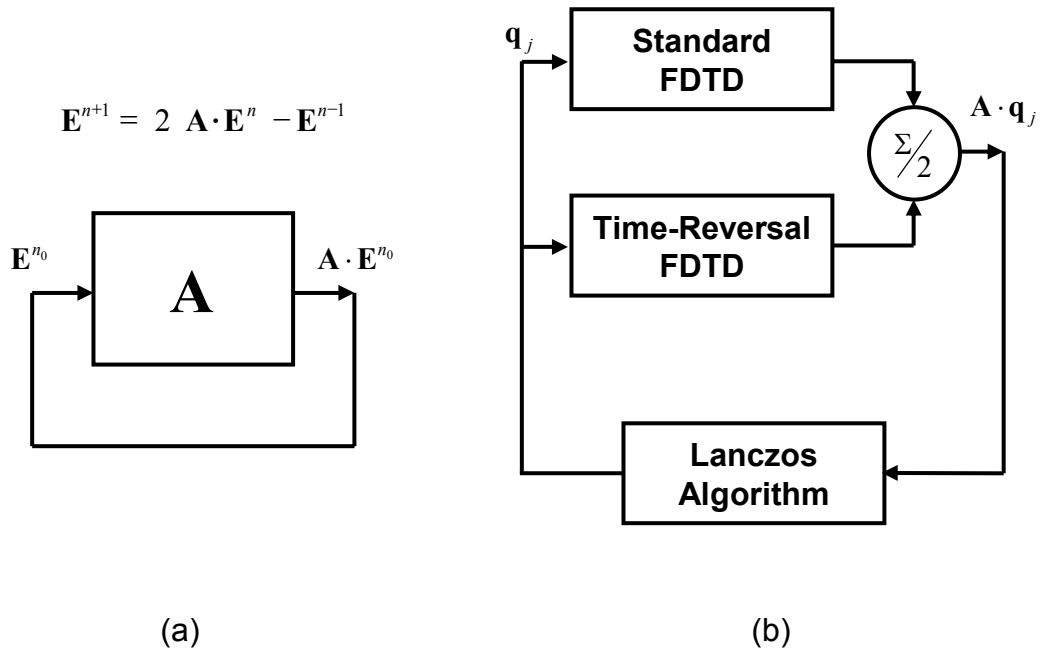


Fig. 3.2 Model-order reduction by time-reversal FDTD and Lanczos algorithm applying to (3.2a). (a) Block diagram for the direct computing loop of (3.2a). (b) Block diagram for the model-order reduction loop with $\mathbf{q}_1 = \mathbf{E}^{n_0}$.

- 3) At the k -th Lanczos iteration, let $\tilde{\mathbf{E}}^n = \mathbf{q}_k$, calculate $\mathbf{A} \cdot \mathbf{q}_k$ by (3.4) – (3.6).
- 4) Perform all operations for the k -th Lanczos iteration.

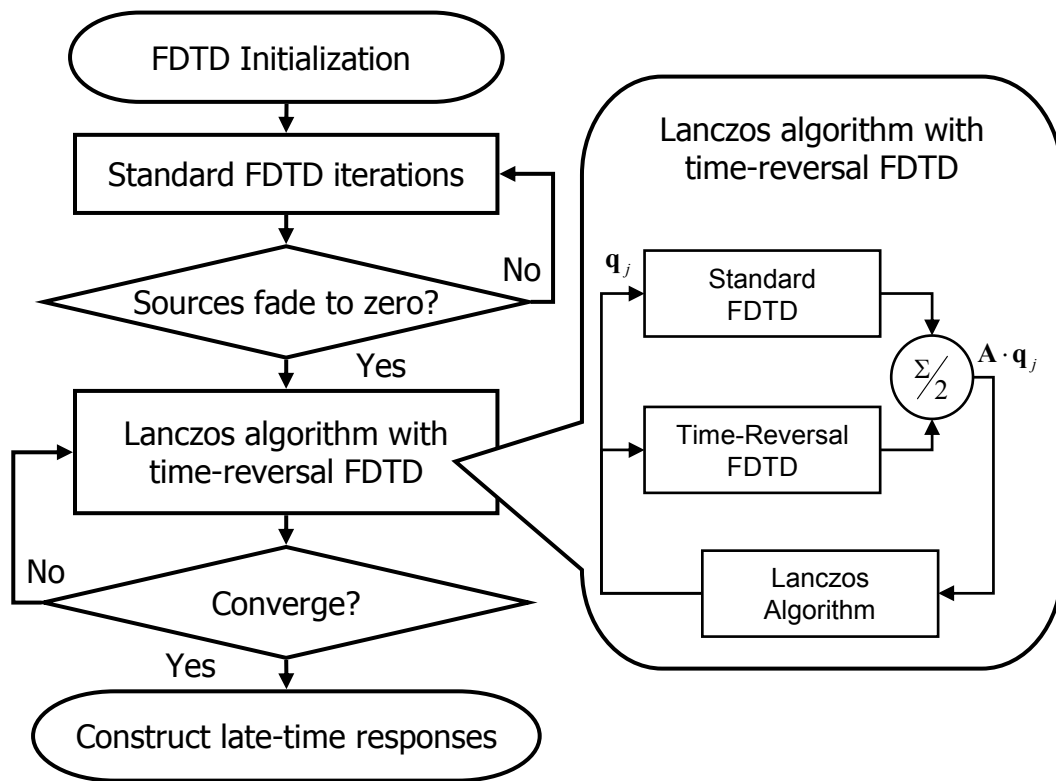


Fig. 3.3. The flow chart of the hybrid method proposed in this chapter, where the matrix-vector product of the Lanczos algorithm is accomplished by standard and time-reversal FDTD, as shown in Fig. 3.2.

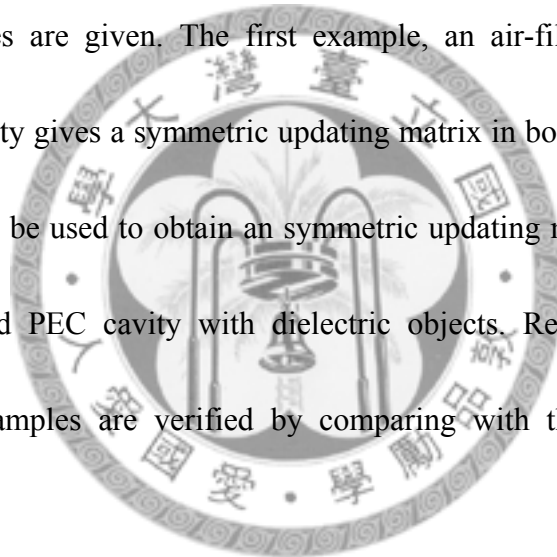
- 5) Solve the eignesolution of \mathbf{T}_k and find the approximate eigenvectors for the original system by (2.20).
- 6) Compute the projection of \mathbf{E}^{n_0} on each eigenvector.
- 7) Repeat 3) – 6) until the projection of \mathbf{E}^{n_0} on the newly added eigenvector

is negligible.

- 8) Solve (3.3) for each approximate eigenpairs.
- 9) Obtain the approximate solution for the steady-state response of the original system.

In order to verify the hybrid method associated with both equations in (3.2).

Two simple examples are given. The first example, an air-filled perfect electric conductor (PEC) cavity gives a symmetric updating matrix in both (3.2a) and (3.2b), while only (3.2b) can be used to obtain an symmetric updating matrix in the second example, an air-filled PEC cavity with dielectric objects. Results of the hybrid method for both examples are verified by comparing with those of brute-force FDTD.



3.2 Homogeneous PEC Cavity

3.2.1 Simulation Settings

Fig. 3.4 shows the geometry of the first example, an air-filled PEC cavity of dimension 10 cm by 10 cm by 1 cm. The size of spatial division for FDTD

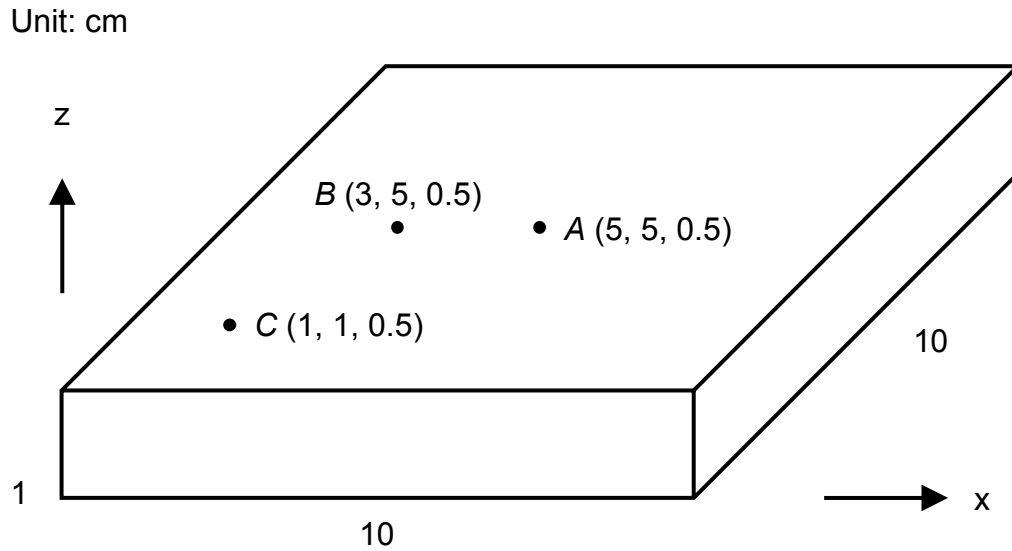


Fig. 3.4 An air-filled PEC cavity of dimension 10 cm by 10 cm by 1 cm.

simulation in each direction is 1 cm and the normalized time step $c \cdot \Delta t$ is 0.5 cm, where c is the velocity of light in free space. A z -directed electric field excitation of Gaussian pulse $\exp(-(c \cdot t - 50.5)^2 / 100)$ (volt/m) is applied at the point A in Fig. 3.4, the center of the cavity. For the hybrid method, iterations of Lanczos algorithm begins after the source fades to zero with additional time margin for the round-trip time.

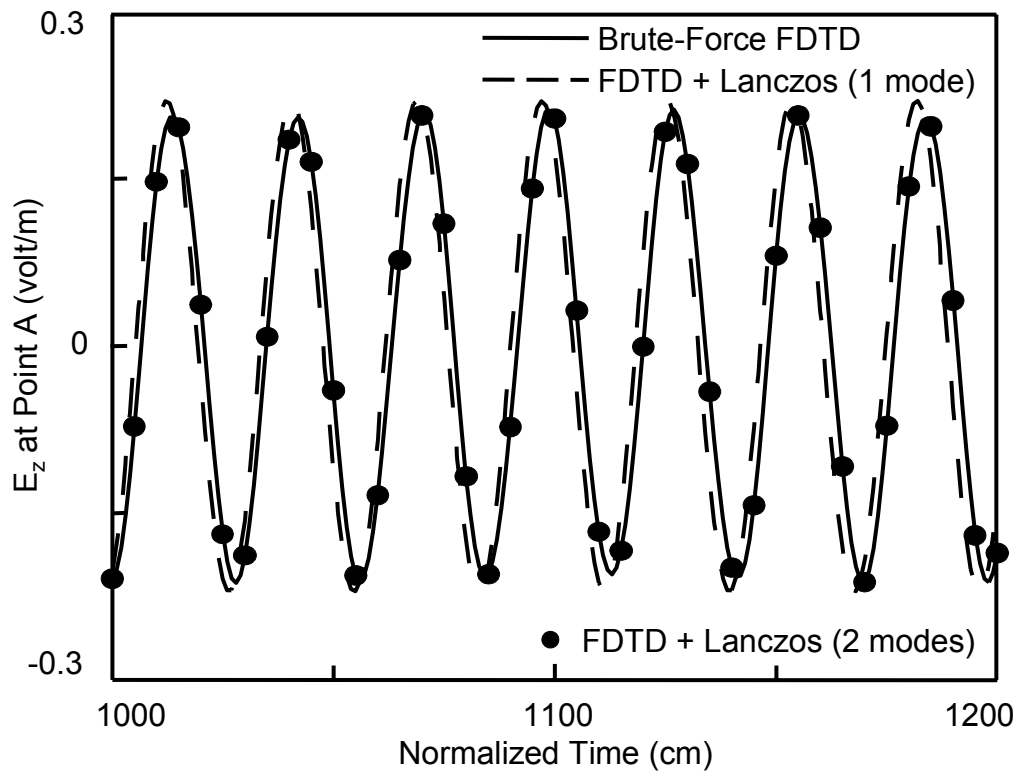


Fig. 3.5. The late-time responses of the z -component of the electric field at point A obtained by brute-force FDTD and the hybrid method with different numbers of modes extracted.

3.2.2 Late-Time Responses

The late-time responses of the z -component of the electric field E_z observed at the points A , B , and C in Fig. 3.4 obtained by FDTD method and the hybrid method are shown in Fig. 3.5 and 3.5. Fig. 3.5 compares E_z at the point A in Fig. 3.6

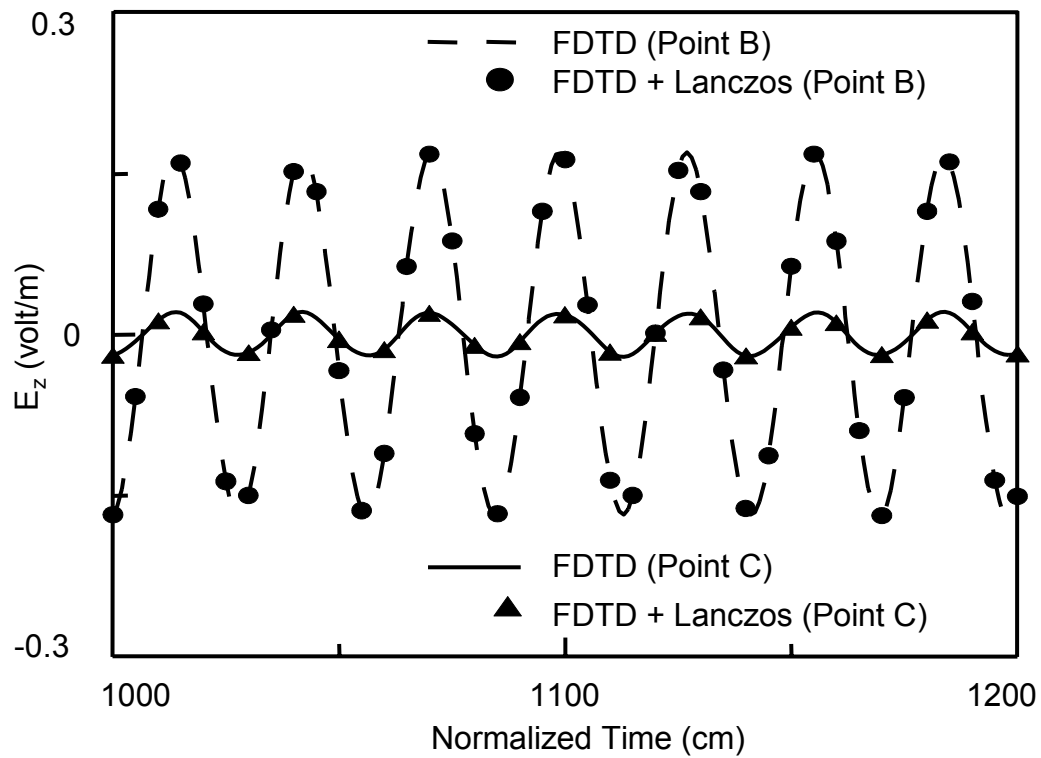


Fig. 3.6. The late-time responses of the z-component of the electric field at points B and C obtained by brute-force FDTD and the hybrid method with two modes extracted.

obtained by brute-force FDTD and the hybrid method with different numbers of modes extracted. As indicated by the figure, the steady-state response is faithfully reconstructed in this case with only two modes extracted in the hybrid method. Fig. 3.6 shows the steady-state response of E_z at another two points B and C in Fig. 3.6 which are obtained by FDTD and the hybrid method with two modes extracted. The

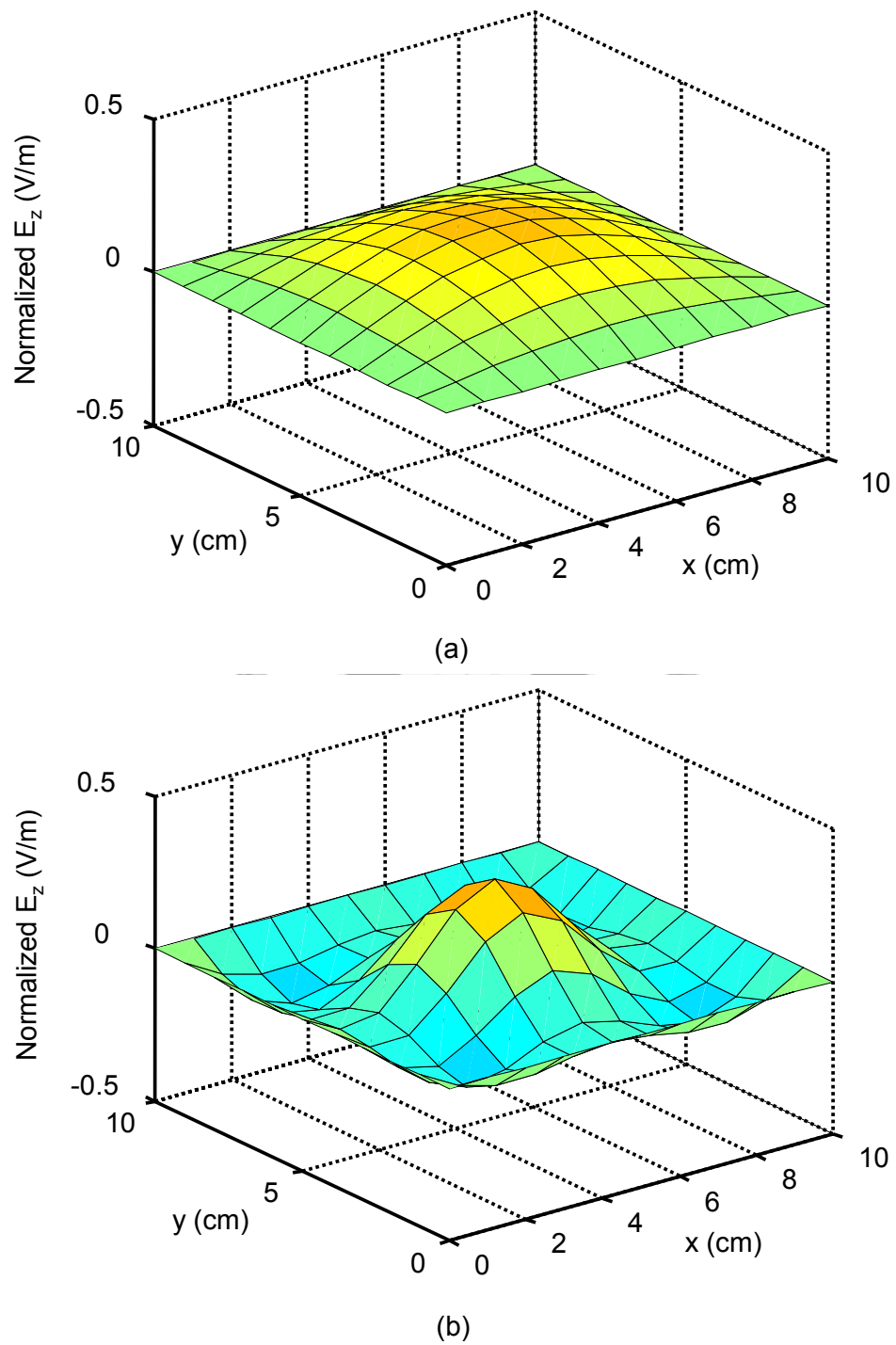


Fig. 3.7. Modal patterns of the first two modes extracted by Lanczos algorithm. (a) The first mode extracted; (b) the second mode extracted.

results are once again in good agreement.

3.2.3 Modal Patterns

Fig. 3.7 shows the modal patterns of the first two modes extracted by Lanczos algorithm. The normalized z -component of the electric field at plane $z=0.5\text{cm}$ in the cavity is plotted. Due to the excitation symmetry, the first two modes extracted by Lanczos algorithm are TM_{110} (Fig. 3.7a) and TM_{330} (Fig. 3.7b). In other words, modes which are not excited will be effectively neglected by Lanczos algorithm. For the cases with nearly degenerate modes that are usually difficult to handle with common extrapolation techniques, it can be easily handled by the proposed hybrid method. By dealing with the modes of the original system, degenerate modes can be easily distinguished since their modal patterns are orthogonal.

3.3 Inhomogeneous PEC Cavity

3.3.1 Simulation Settings

The geometry of the second example, an air-filled PEC cavity with a dielectric object, is shown in Fig. 3.8. The dimension of the cavity is 30mm by 50mm by

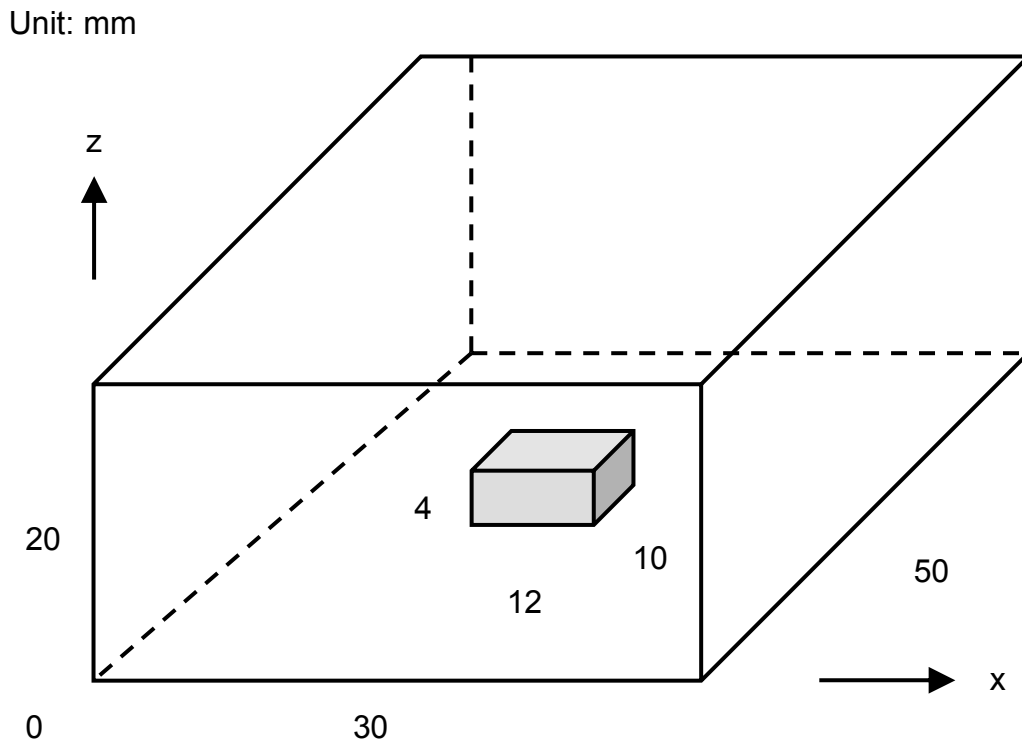


Fig. 3.8. An air-filled PEC cavity with a dielectric object.

20mm. The dielectric object locates at the bottom center of the cavity which is 12 mm by 10 mm by 4 mm in size with a relative permittivity 4.0. The spatial division is 1 mm in all directions and the time step is chosen to be 1.6 ps.

The cavity is excited with a z -directed electric field source at the plane $y = 40$ mm in the form of Gaussian pulse. For a symmetric updating matrix, the hybrid method associated with (3.2b) is used. Two pulses with different rise times,

$\exp(-(n-250)^2/50^2)$ (volt/m) and $\exp(-(n-125)^2/25^2)$ (volt/m) with n denoting the FDTD time step, are applied for verifying the convergence criteria which will be described in the next section.

3.3.2 Late-Time Responses

For the pulse with longer rise time, Lanczos algorithm begins at the 800-th time step, i.e., after the source fades to zero with additional round-trip time for the excitation. Only four modes are needed to be precisely extracted and the hybrid method converged at the sixth Lanczos iteration. Fig. 3.9a shows the steady-state response of the y -component of the magnetic field observed at the point (0.5 mm, 10 mm, 10 mm) and Fig. 3.9b shows that of the x -component of the magnetic field observed at the point (15 mm, 0.5 mm, 10 mm) in Fig. 3.8, which are excited by the source with a longer rise time.

If the pulse with a shorter duration is used for the excitation instead, Lanczos algorithm can be applied earlier in the hybrid method since the source fades to zero much faster. For the Gaussian pulse with a shorter rise time described in the previous paragraphs, Lanczos algorithm begins at the 600-th time step. However, more modes

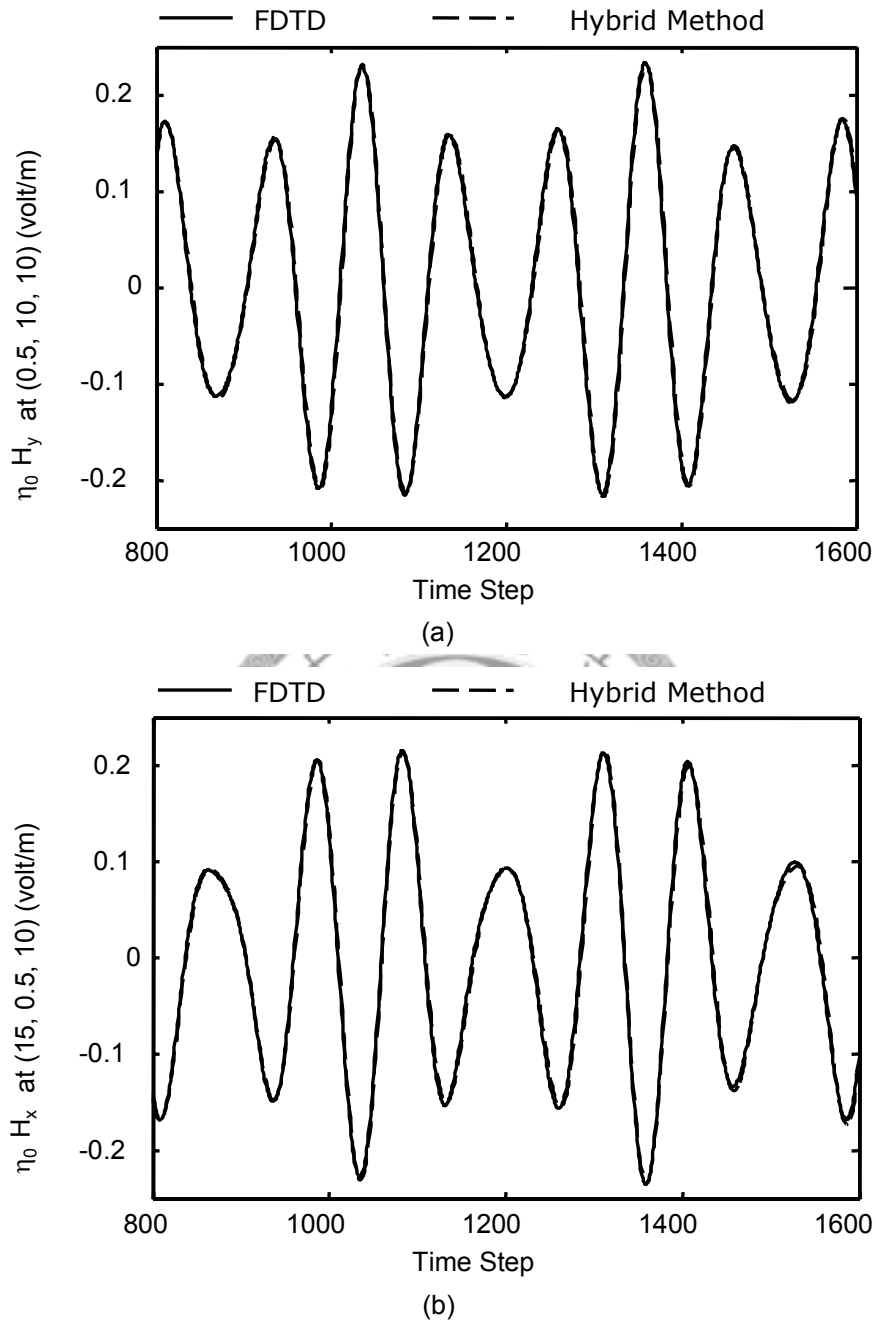


Fig. 3.9. The late-time responses of (a) the y-component at the point (0.5 , 10 , 10)(mm) and (b) the x-component at the point (15 , 0.5 , 10)(mm) of the magnetic field in Fig. 3.5 which is excited by a Gaussian pulse with a longer rise time.

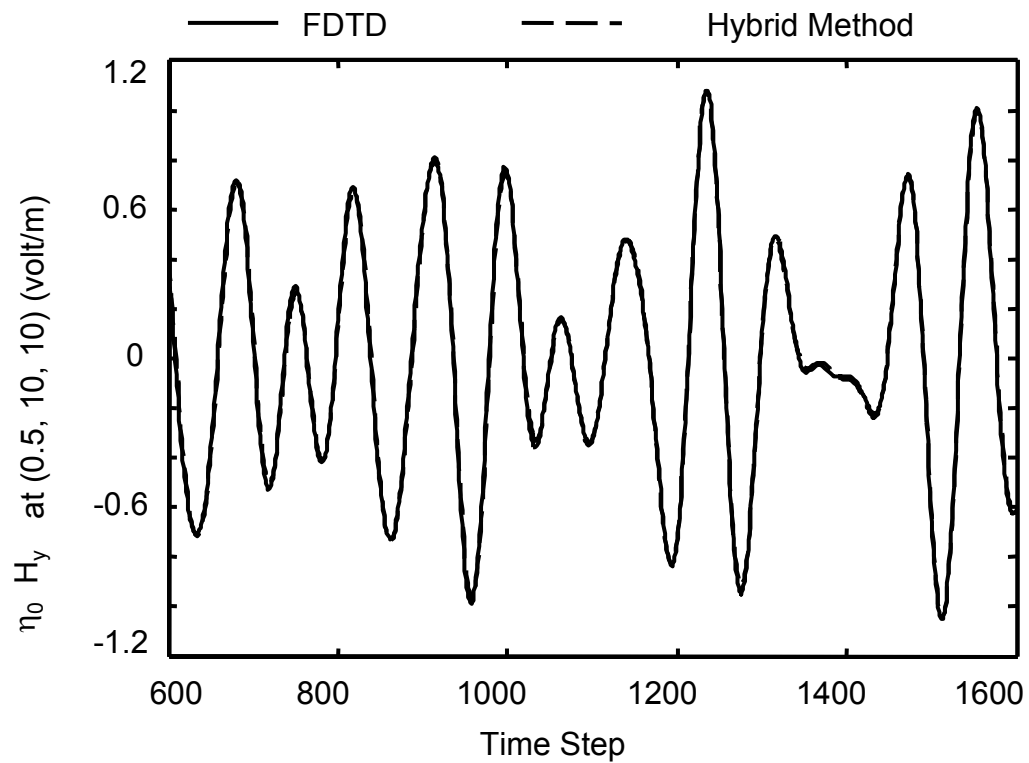


Fig. 3.10. The late-time responses of the y-component of the magnetic field at the point (0.5 mm, 10 mm, 10 mm) in Fig. 4 which is excited by a Gaussian pulse with a shorter rise time.

are needed to be extracted precisely because higher modes are excited.

Fig. 3.10 shows the result obtained by FDTD and the hybrid method. With the first six modes converged at the fifteenth Lanczos iteration in the hybrid method, the steady-state response of the y-component of the magnetic field observed at the point

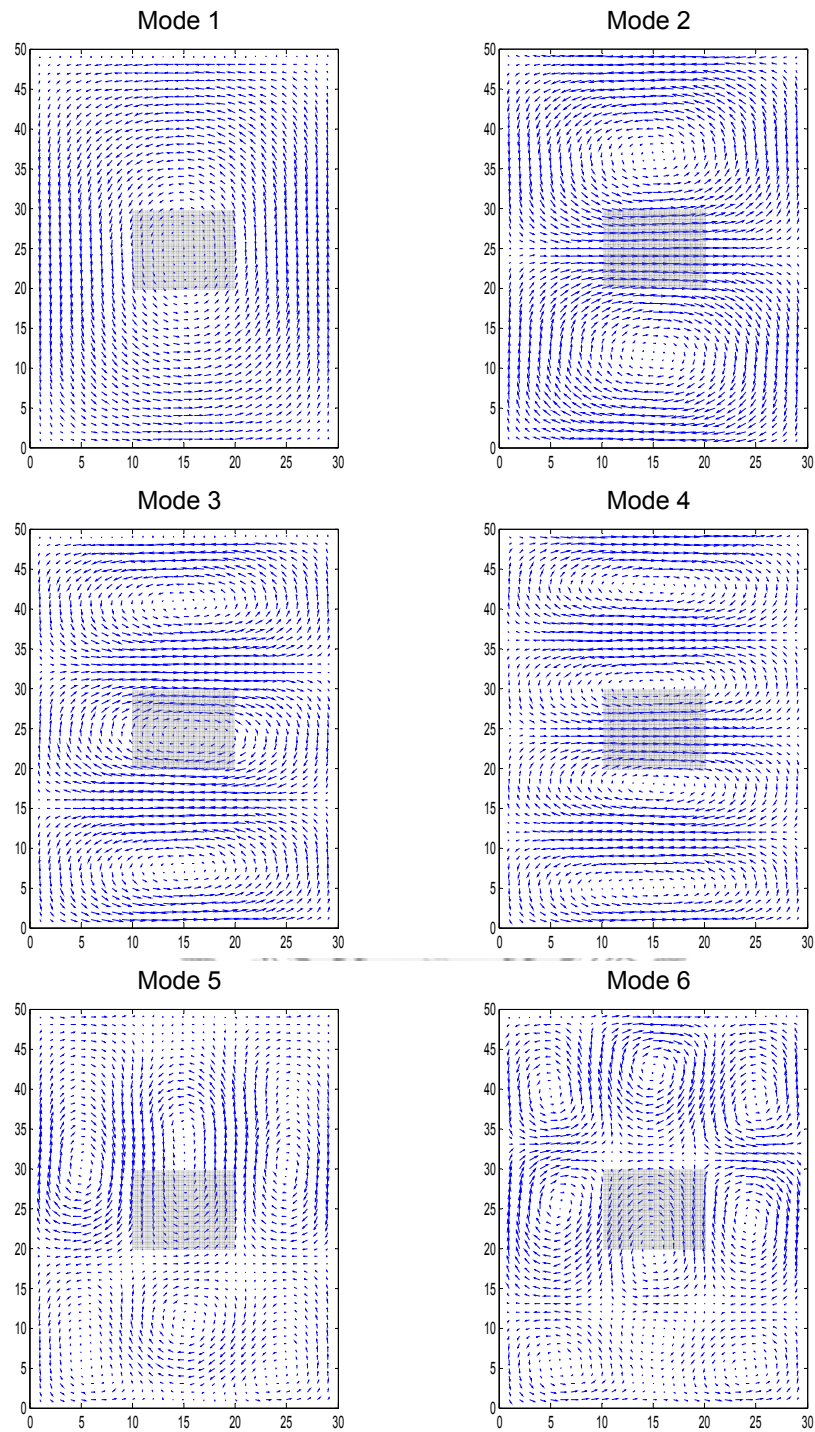
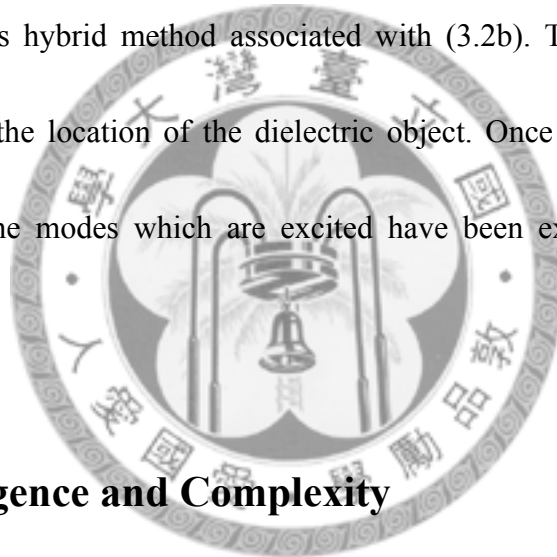


Fig. 3.9. Modal patterns of the magnetic field at the $z = 10\text{mm}$ plane in the structure shown in Fig. 3.8 for the first six modes extracted by Lanczos algorithm.

(0.5 mm, 10 mm, 10 mm) in Fig. 3.8 which is excited by the source with a shorter rise time is reconstructed faithfully.

3.3.3 Modal Patterns

Fig. 3.11 shows the modal patterns of the magnetic field at the $z=10\text{mm}$ plane in the structure shown in Fig. 3.8 for the first six modes which are extracted by the FDTD/Lanczos hybrid method associated with (3.2b). The shaded rectangular region represents the location of the dielectric object. Once again it can be easily found that only the modes which are excited have been extracted by the hybrid method.



3.4 Convergence and Complexity

As described in the previous section, the hybrid method is able to give a good approximation for the steady-state response of the original problem with only a few modes extracted in a few Lanczos iterations. It is important to determine the convergence criteria about the number of modes which is necessarily to be concerned and how precisely should these modes be extracted. It is also an important issue to analyze the complexity of the hybrid method. The second case in the previous section

will be used as an example for discussing the convergence and complexity issues in the following paragraphs.

3.4.1 Convergence

As described in step 6) in the step-by-step implementation that summarized 3.1, in order to determine the number of modes that are needed to be extracted precisely, the expansion coefficients of the eigenmodes are compared. After m Lanczos iterations, an approximate eigensolution set of the original system can be found by (2.20). The expansion coefficient a_i associated with θ_i is calculated by taking the inner product with the field vectors \mathbf{E}^{n_0} or \mathbf{H}^{n_0} at the n_0 -th time step of FDTD iteration that the Lanczos algorithm starts. Terms with small expansion coefficient can then be dropped safely.

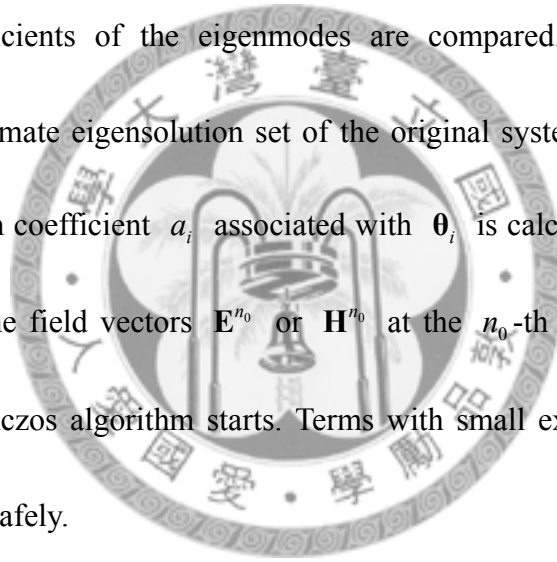


Fig. 3.12 shows the absolute value of the smallest expansion coefficient a_{\min} normalized to the largest one, a_{\max} , which is obtained at each of the Lanczos iteration in the second example described in the previous section. One can see that after certain iterations, the smallest expansion coefficient decays to tenth an order of the largest one. Therefore number of modes to be precisely extracted is determined.

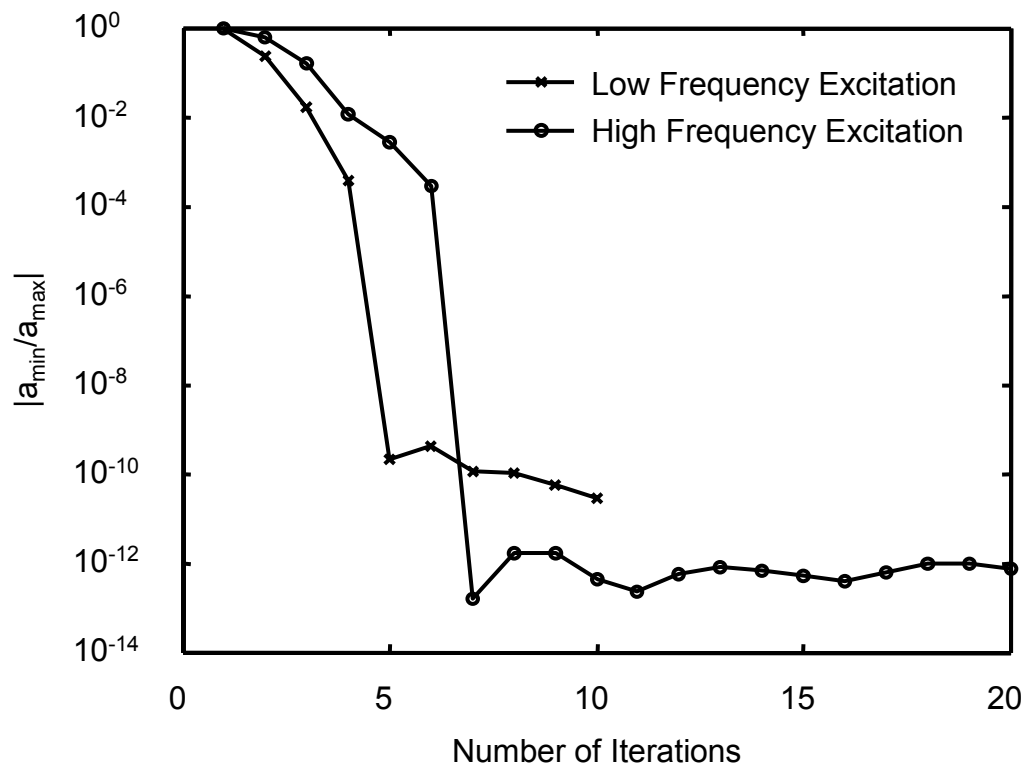


Fig. 3.12. The absolute value of the smallest expansion coefficient a_{\min} normalized to the largest one, a_{\max} , which is obtained at each of the Lanczos iteration in the second example described in the previous section.

For example, only four modes are needed to be precisely extracted when the system is excited by the lower frequency source, while six modes should be taken into consideration with the higher frequency excitation. The Lanczos iteration terminates when all of the concerning modes have been extracted with the desired precisions.

3.4.2 Complexity

To obtain a frequency response with a higher resolution in frequency, a longer time period of steady-state response in time-domain should be obtained. In traditional FDTD simulation, fine meshes in spatial leads to small division in time. As a result, more simulation time is needed for better frequency resolution.

Assume that there are P field points in an FDTD simulation. It takes L time steps for the sources fade to zero and the modal patterns begin to appear and after that N time steps are performed for a satisfactory frequency resolution. The overall computation time for standard FDTD is linearly proportional to the number of field points and total time step computed, or $O(P \cdot (L + N))$.

For the proposed hybrid method, standard FDTD is firstly applied for the same L time steps. Lanczos algorithm is then applied for model-order reduction. Assume that Q modes need to be extracted precisely and the Lanczos algorithm converges at the M -th time step. For each Lanczos iteration, at most Q modal expansion coefficients are obtained and the eigensolution of the $m \times m$ tridiagonal matrix is also solved for the convergence criteria.

After that, the frequency response at a single field point with the same resolution can be directly obtained with multiplications of order N . The overall complexity of the hybrid method is therefore $O(P \cdot L + Q \cdot N + M^2)$. In the usual cases, $Q \leq M \ll L \ll N \ll P$, thus the standard FDTD has a $O(P \cdot N)$ complexity, where as the hybrid method reduces the complexity to $O(P \cdot L)$, i.e., a speed up factor $\frac{N}{L}$ can be achieved. For structures with enormous active modes, e.g. optical waveguides or photonic crystals, the speed up factor may be reduced if $O(M^2)$ eventually reaches $O(P \cdot L)$.

In comparison with common extrapolation techniques, e.g., Prony's methods [2], [4], [5], utilization of space information make Lanczos iterations able to be applied earlier, as long as the sources have faded to zero and the electromagnetic wave has spread over the computation domain. Utilization of space information also make the hybrid method converges much more rapidly. In addition, the reduced model obtained by this hybrid method is able to predict the late-time responses at any points of the original system without increasing computational overheads. For the Prony's methods, this can only be done with enormous sampling points at both time and space grids.

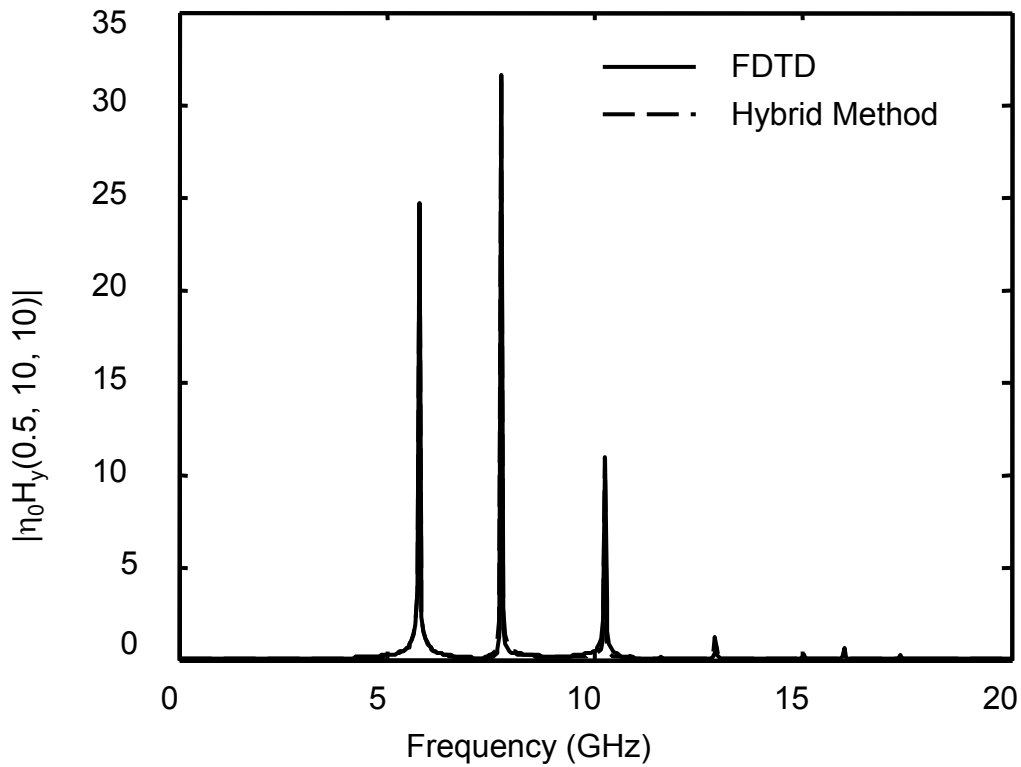
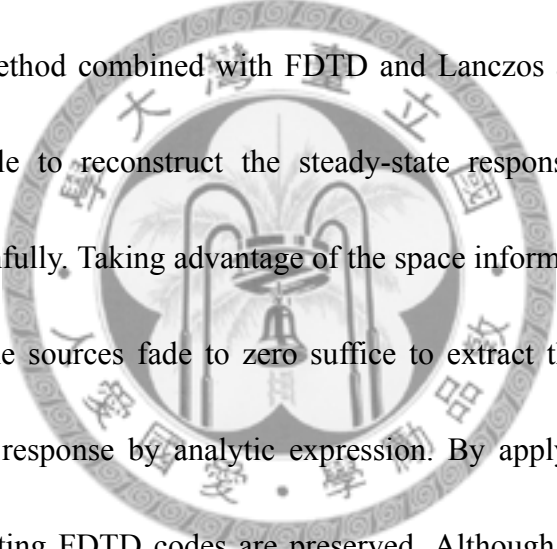


Fig. 3.13. The magnitude of the frequency response of the magnetic field obtained at the point (0.5 mm, 10 mm, 10 mm) in Fig. 4 in the second example in IV with a high frequency excitation.

Fig. 3.13 shows the magnitude of the frequency response of the magnetic field obtained at the point (0.5 mm, 10 mm, 10 mm) in Fig. 3.8 with a high frequency excitation. In order to obtain a 40 MHz frequency resolution, 16001 time steps are performed in the standard FDTD method. In this case, $P = 30000$, $N = 15401$, $L = 600$, $M = 15$, and $Q = 6$. The results of both methods are once again in good

agreement. Moreover, total solution time for the standard FDTD computation is 128 minutes while only 5.1 minutes are spent for the hybrid method, about 25 times faster. This also agrees with the complexity analysis in the previous paragraph, i.e., $N/L \approx 25$.

3.5 Summary of the Chapter



The hybrid method combined with FDTD and Lanczos algorithm proposed in this chapter is able to reconstruct the steady-state response of a large system efficiently and faithfully. Taking advantage of the space information, only few FDTD iterations before the sources fade to zero suffice to extract the excited modes and then the late time response by analytic expression. By applying the time-reversal technique, the existing FDTD codes are preserved. Although suitable for problems with non-magnetic material only, the hybrid method still applies in common problems. With two simple examples, the correctness, efficiency, convergence, and complexity of this method have been verified for closed systems.



4

Late-Time Response for Delaunay-Voronoi Modeling of Power-Ground Planes in Time-Domain with Krylov Subspace Method

DELAUNAY-Voronoi modeling of power-ground planes in time-domain discussed in 2.2 is combined with Krylov subspace method in this chapter for efficiently obtaining the steady-state response for the power-ground plane problems. The updating equations are treated in a similar manner as FDTD to get a symmetric updating matrix. Krylov subspace method based on Lanczos algorithm is applied to the symmetric updating matrices after the sources fade to zero.

Detailed derivation of the hybrid method is described in the first section, followed by numerical examples including a simple square power-ground plane with various mesh settings and a more realistic case of power-ground plane with a clipped corner and an aperture on the plane. Convergence and complexity of the hybrid method will also be discussed before the summary of this chapter.

4.1 Krylov Subspace Method for Delaunay-Vononoi Modeling of Power-Ground Planes in Time-Domain

The time marching scheme of Delaunay-Vononoi modeling of power-ground planes in time-domain has been introduced in 2.2. In order to obtain the late-time response with minimum iterations in updating (2.12), a similar model-order reduction procedure as that described in chapter 3 is applied to the system after the sources fades to zero with a little margin of round-trip time. Active modes in the system are extracted for the reconstruction of the late-time response without actually update (2.12) to the time desired.

Starting from (2.12), if the node voltages V_i^n and the branch currents flowing through the series inductance connecting the i - and j -th nodes $I_{ij}^{n+\frac{1}{2}}$ are rewritten as column vectors, the updating equations can be cast into matrix form

$$\begin{bmatrix} \mathbf{V}^n \\ \mathbf{I}^{n+\frac{1}{2}} \end{bmatrix} = \begin{bmatrix} \mathbf{I} & \mathbf{D}_I \\ \mathbf{D}_V & I + \mathbf{D}_V \mathbf{D}_I \end{bmatrix} \begin{bmatrix} \mathbf{V}^{n-1} \\ \mathbf{I}^{n-\frac{1}{2}} \end{bmatrix}. \quad (4.1)$$

Rows associated with the branch currents in (4.1) can be eliminated to get an update equation with node voltages

$$\mathbf{V}^{n+1} = 2\mathbf{A} \cdot \mathbf{V}^n - \mathbf{V}^{n-1}, \quad (4.2)$$

$$K^m = \{ \mathbf{b}, \mathbf{A}\mathbf{b}, \mathbf{A}^2\mathbf{b}, \dots, \mathbf{A}^{m-1}\mathbf{b} \} \Rightarrow \mathbf{Q}_m, \mathbf{T}_m, \quad \mathbf{A}\mathbf{Q}_m = \mathbf{Q}_m\mathbf{T}_m$$

$$\mathbf{V}^{n+1} = 2\mathbf{A} \cdot \mathbf{V}^n - \mathbf{V}^{n-1}$$

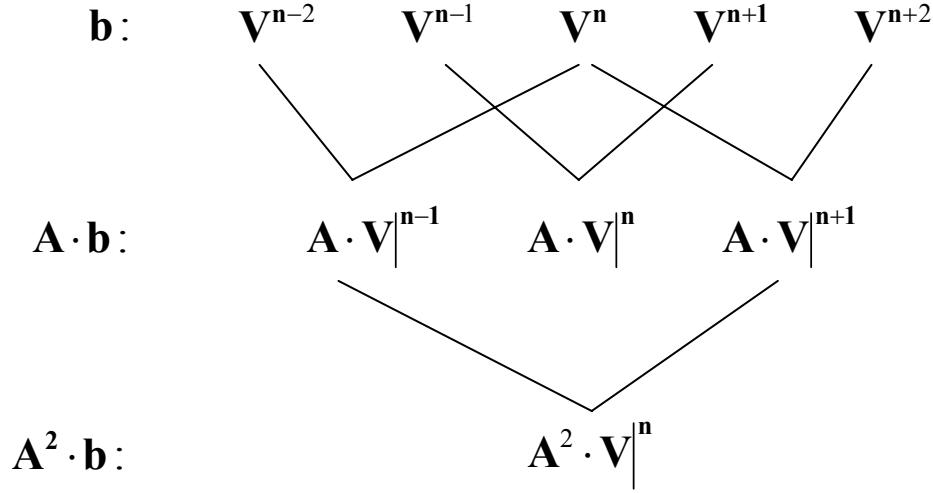


Fig. 4.1. Constructing a Krylov subspace for the approximation of system matrix \mathbf{A} directly from a series of system response in time.

where $\mathbf{A} = \left[I + \frac{1}{2} D_I D_V \right]$ is a symmetric matrix. Applying Lanczos algorithm to \mathbf{A} with exactly the same method in chapter 3 requires the time-reversal expression of (2.12) and is not preferred here. Instead, the hybrid method proposed in this chapter constructs a Krylov subspace directly from the output results of the time domain iterations with the basic idea shown in Fig. 4.1. Comparing to the FDTD/Lanczos hybrid method, this hybrid technique is able to deal the cases without source codes of

time-domain full-wave solvers, provided the field information at any time steps is obtainable.

As indicated by (4.2), if the column vector of the node voltage \mathbf{V}^{n_0} at some time step n_0 is chosen as the starting vector \mathbf{b} of a Krylov subspace, the second vector of the Krylov subspace $\mathbf{A}\mathbf{b}$ can be obtained by averaging the voltage vectors at the previous and the next time steps as

$$\mathbf{A} \cdot \mathbf{b} \Big|^{n_0} = \mathbf{A} \cdot \mathbf{V}^{n_0} = \frac{1}{2} (\mathbf{V}^{n_0+1} + \mathbf{V}^{n_0-1}), \quad (4.3)$$

where the superscript n_0 indicates that the Krylov subspace is constructed with the node voltage at time step n_0 as the starting vector. Applying the system operator \mathbf{A} to (4.3), the next vector of the Krylov subspace $\mathbf{A}^2\mathbf{b}$ can be derived.

$$\begin{aligned} \mathbf{A}^2 \cdot \mathbf{b} \Big|^{n_0} &= \mathbf{A} \cdot (\mathbf{A} \cdot \mathbf{V}^{n_0}) \\ &= \frac{1}{2} (\mathbf{A} \cdot \mathbf{V}^{n_0+1} + \mathbf{A} \cdot \mathbf{V}^{n_0-1}) \\ &= \frac{1}{2} (\mathbf{A} \cdot \mathbf{b} \Big|^{n_0+1} + \mathbf{A} \cdot \mathbf{b} \Big|^{n_0-1}) \end{aligned} \quad (4.4)$$

In general, the m -th vector of the Krylov subspace constructed with the node voltage at time step n_0 can be obtained by averaging the $(m-1)$ -th vector of the Krylov subspaces constructed with the node voltage at time steps n_0+1 and n_0-1 , or more specifically,

$$\mathbf{A}^{m-1} \cdot \mathbf{b} \Big|^{n_0} = \frac{1}{2} \left(\mathbf{A}^{m-2} \cdot \mathbf{b} \Big|^{n_0+1} + \mathbf{A}^{m-2} \cdot \mathbf{b} \Big|^{n_0-1} \right). \quad (4.5)$$

The hybrid method begins with the standard iteration of the updating equations (2.12). After the sources fade to zero and a little time margin for the round-trip time of the propagating wave, the voltage distribution on the power-ground planes will gradually become a linear combination of a few dominant modes.

In order to construct a Krylov subspace of an order at most m with the node voltage at time step n_0 as a starting vector, the node voltages from its previous $m-1$ time steps to its next $m-1$ time steps is stored. Applying (4.5) to the stored voltage vectors iteratively, a series of Krylov subspaces $\kappa^k(\mathbf{A}, \mathbf{V}^{n_0})$ of orders $k=1, 2, \dots, m$ as well as their Lanczos vectors \mathbf{Q}_k and tridiagonal matrices \mathbf{T}_k can be construct for the approximation of the original system matrix \mathbf{A} with (2.20).

If the expansion coefficient corresponding to the j -th eigenvector at n -th time step in the iterations is denoted by $a_{n,j}$, the following recurrence relation can be obtained by substitution of the expansion coefficients to (4.2),

$$a_{n+1,j} - 2\lambda_j a_{n,j} + a_{n-1,j} = 0, \quad (4.6)$$

where λ_j is the corresponding j -th eigenvalue of the updating matrix in (4.2).

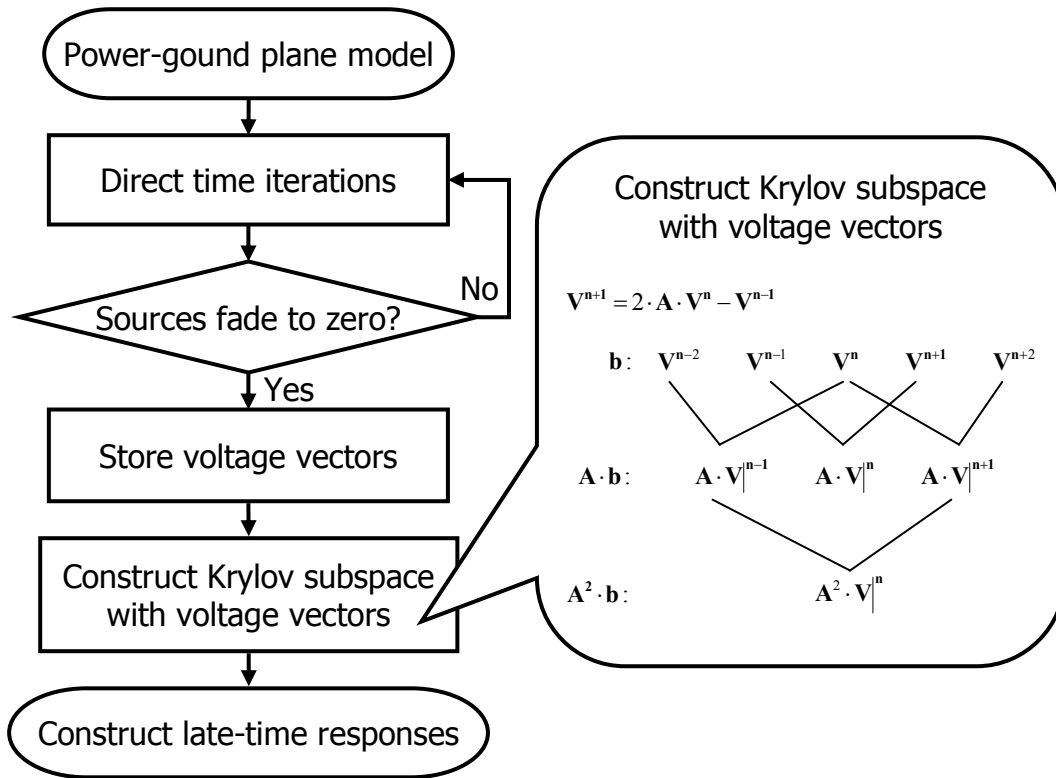


Fig. 4.2. Flow chart of the hybrid method proposed in this chapter, where the Krylov subspace is constructed directly from the pre-stored voltage vectors as shown in Fig. 4.1.

The second order difference equation in (4.6) can be solved analytically if λ_j and two initial conditions, $a_{n_0,j}$ and $a_{n_0-1,j}$ are given for some time step n_0 . Once (4.6) is solved, the expansion coefficient $a_{n,j}$ at any time step $n \geq n_0 - 1$ can be calculated directly. This can be done for the most significant k -th eigenvectors. Then an approximate solution for the steady-state response of the original large system can

be obtained analytically.

Penalty of the proposed hybrid method comes when the Krylov subspaces do not converge before running out of the stored voltage vectors. Standard iteration by (2.12) is then restart for more successive voltage vectors, after that a new Krylov subspace with a starting vector at the middle time step of the voltage vector series is needed to be reconstructed.

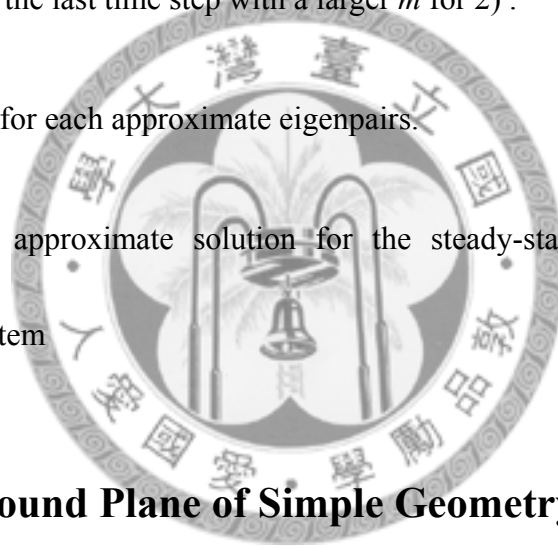
Figure 4.2 shows the flow chart of the hybrid method proposed in this chapter. For clarity, the hybrid method is summarized as follows.

- 1) Construct the equivalent circuit network according to the mesh setting for a structure using Delaunay-Vononoi modeling.
- 2) Perform the standard iterations (2.12) until all sources fade to zero with additional round-trip time according to the system dimension.
- 3) Store all \mathbf{V}^n 's for $n_0 - m + 1 \leq n \leq n_0 + m - 1$.

For the starting vector $\mathbf{b} = \mathbf{V}^{n_0}$,

- 4) Construct a k -th order Krylov subspace $\kappa^k(\mathbf{A}, \mathbf{V}^{n_0})$ by 4.5 and obtain its Lanczos vectors \mathbf{Q}_k and tridiagonal matrices \mathbf{T}_k .

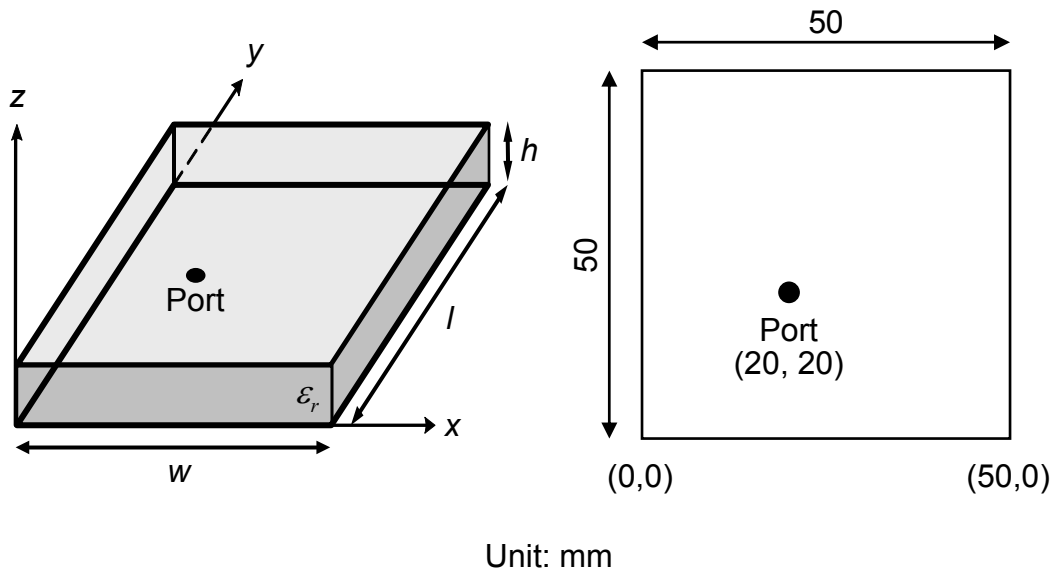
- 5) Solve the eignesolution of \mathbf{T}_k and find the approximate eigenvectors for the original system by (2.20).
- 6) Compute the projection of \mathbf{V}^{n_0} on each eigenvector.
- 7) Repeat 3) – 6) until the projection of \mathbf{V}^{n_0} on the newly added eigenvector is negligible with $k := k + 1$ if $k \leq m$, otherwise go back to 1) and restart (2.12) from the last time step with a larger m for 2) .
- 8) Solve (3.3) for each approximate eigenpairs.
- 9) Obtain the approximate solution for the steady-state response of the original system



4.2 Power-Ground Plane of Simple Geometry

4.2.1 Geometry

Fig. 4.3 shows a square power plane with $w = l = 50\text{mm}$, $h = 1.6\text{mm}$, and a relative dielectric constant $\epsilon_r = 4.2$. A port is located at $(20\text{mm}, 20\text{mm})$ where a Gaussian current pulse $I_s = I_0 \exp(-(t - t_0)^2 / t_d^2)$, with $I_0 = 1\text{mA}$, $t_0 = 10\text{ns}$, and $t_d = 2\text{ns}$ is injected to excite the structure. With this mesh setting, the late-time



(a)

(b)

Fig. 4.3. The geometry of a 50mm×50mm×1.6mm power-ground plane with an excitation port at (20mm, 30mm). (a) Three-dimensional view. (b) Top view.

responses of the voltage at the port computed directly by (2.12) are compared with the results obtained by the hybrid method described in the previous section. The frequency responses of the input impedance $Z_{in}(f) = \frac{V(f)}{I(f)}$ are also calculated by transforming the time responses of voltage and current into frequency domain with Fast Fourier Transform (FFT).

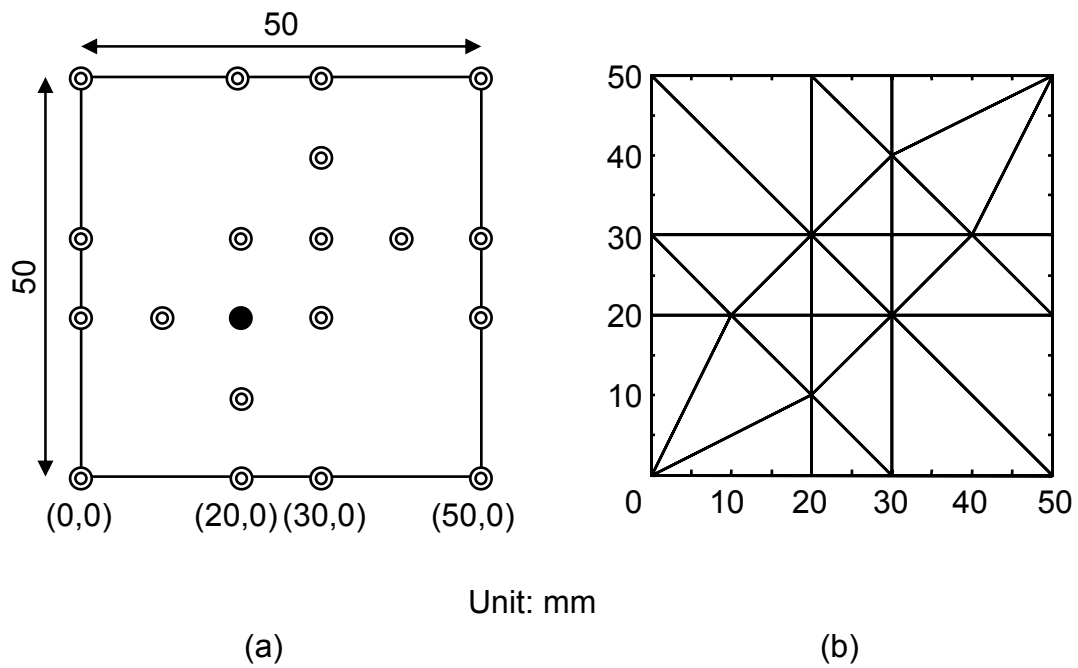


Fig. 4.4. Mesh setting for the simulation of the structure shown in Fig. 4.3. (a) Locations of the input port (solid dot) and virtual ports (double circle). (b) Arrangement of the triangular meshes on the plane.

4.2.2 Simulation Results

Fig. 4.4. shows the mesh setting for the simulation of the structure shown in Fig. 4.3, where the locations of the input port is indicated with a solid dot in Fig. 4.4a and the locations of all virtual ports are plotted with double circles. Triangular

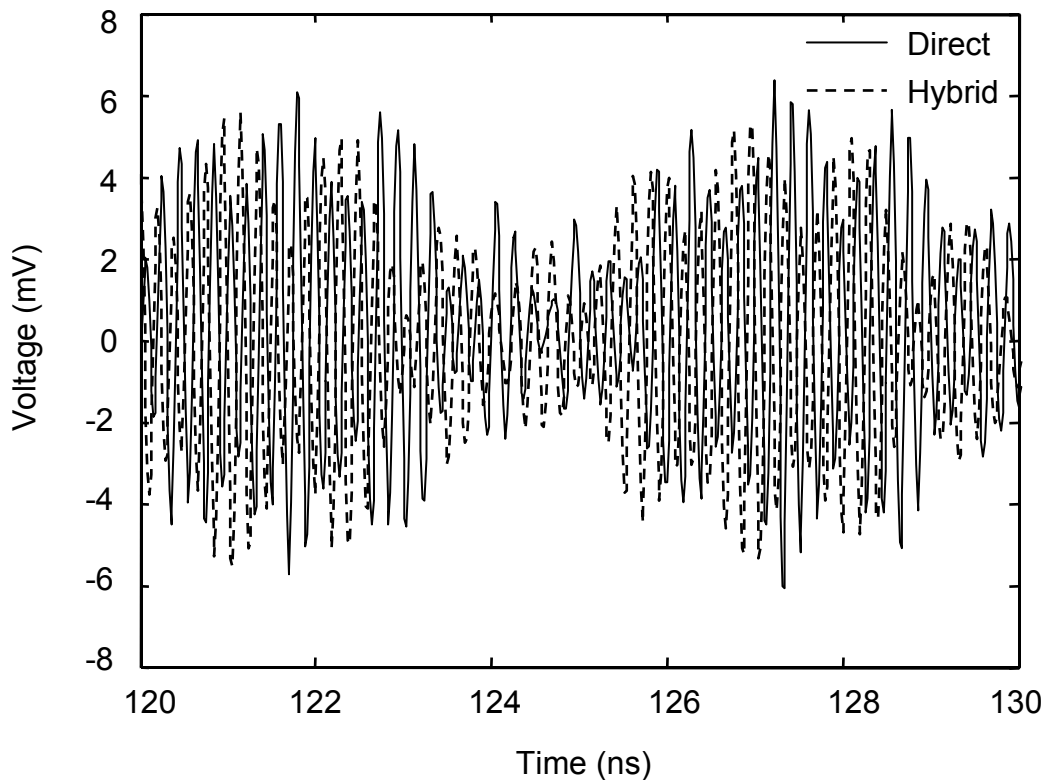


Fig. 4.5. Late-time responses obtained by direct time-domain iteration (solid line) and hybrid method (dashed line) for the structure with a geometry shown in Fig. 4.3 and a mesh settings in Fig. 4.4.

meshes are arranged as shown in Fig. 4.4b. The simulation results obtained by direct time-domain iteration and hybrid method are shown in Fig. 4.5 with a solid and a dashed line, respectively. Obviously quite different results were obtained by the two methods. This could be recognized also in the frequency responses of the input impedance shown in Fig. 4.6, where the solid line represents the result obtained

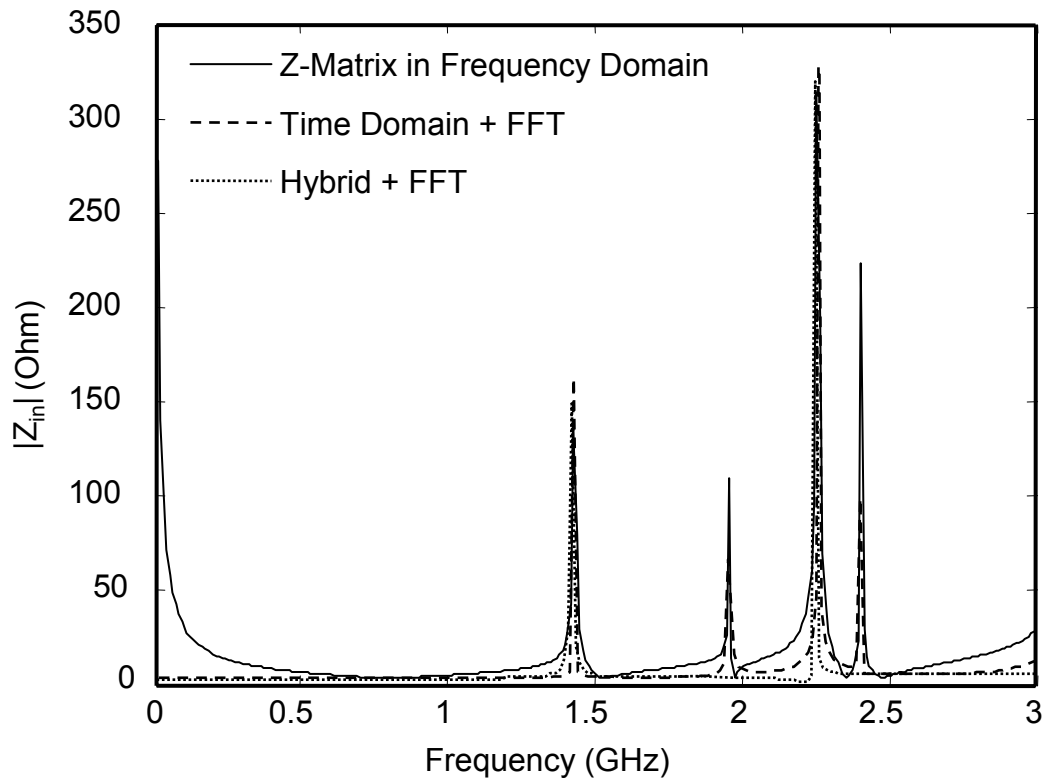


Fig. 4.6. The frequency responses of the input impedance at the port of Fig. 4.3 obtained by direct inverting the Y-matrix in frequency domain (solid line) and the frequency transform by FFT of the late-time responses obtained by direct time-domain iteration (dashed line) and the hybrid method (dotted line).

by direct inverting the Y-matrix in frequency domain. The dashed line and the dotted line are the results of late-time responses transformed into frequency by FFT, which were obtained by direct time-domain iteration and the hybrid method, respectively. One can see that only two of the four resonant frequencies are extracted by the

hybrid method. The explanation of the quite different results, however, can be found by analytical derivation of the resonant frequencies of the structure.

4.2.3 Modal Patterns

For the rectangular cavity shown in Fig. 4.3a, assume that $w, l \gg h$, the cutoff wavenumber of the TM_{mn} mode can be defined [24] as

$$k_{mn} = \sqrt{k_{xm}^2 + k_{yn}^2} \quad (4.7)$$

with $k_{xm} = \left(\frac{m\pi}{w}\right)$ and $k_{yn} = \left(\frac{n\pi}{l}\right)$, where the indices m and n are some integers representing the number of variations in the standing wave pattern in the x and y directions, respectively. The angular frequency of the resonant mode with indices m and n can also be found by

$$\omega_{mn} = v_p \cdot k_{mn}, \quad (4.8)$$

where v_p stands for the phase velocity of light in the dielectric of the resonating cavity. Finally the modal pattern of the voltage at the resonant frequency with indices m and n can be describe by the following formula

$$V_{mn}(x, y, t) = V_{0,mn} \cos(k_{xm}x) \cos(k_{yn}y) \cos(\omega_{mn}t + \phi_{mn}) \quad (4.9)$$

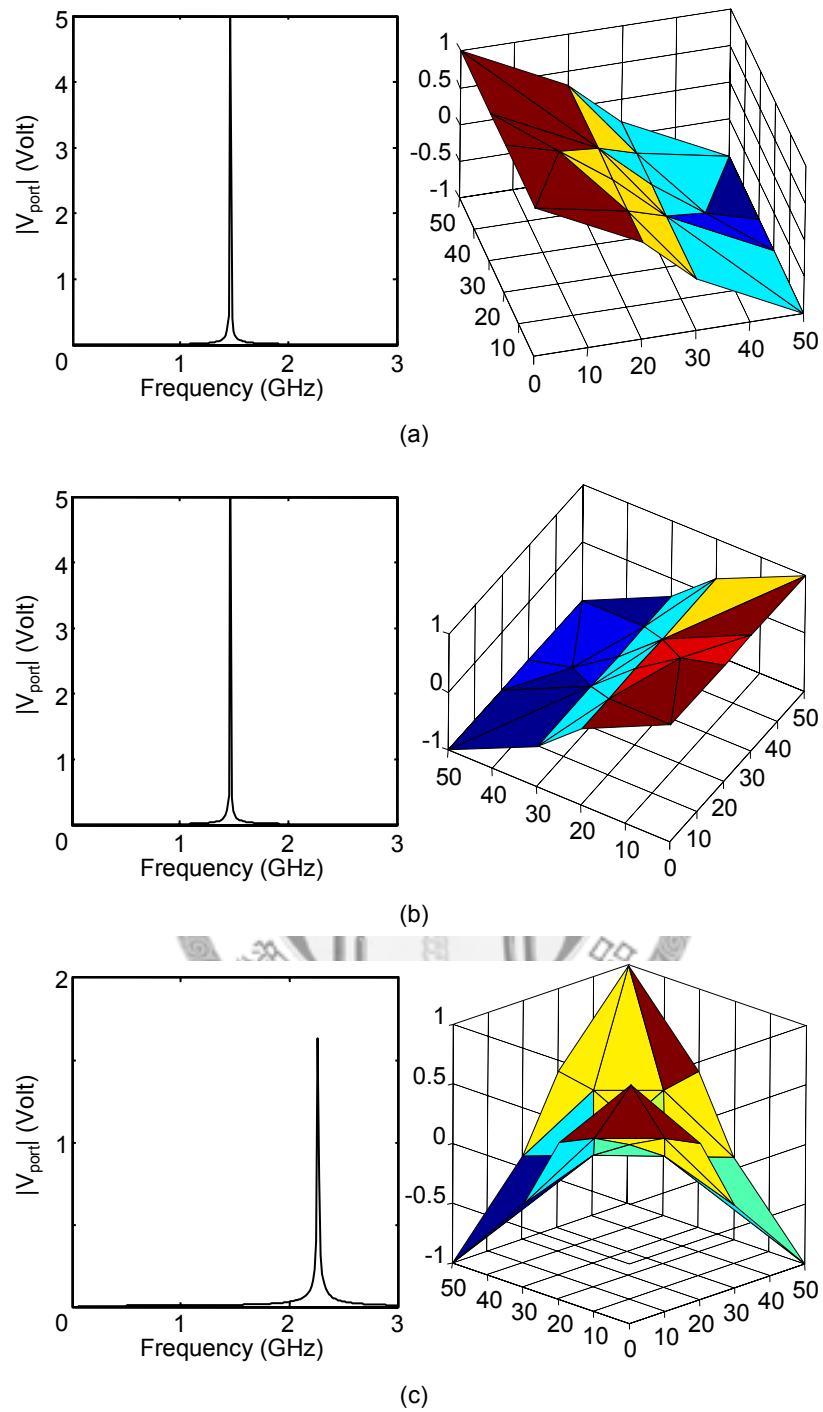


Fig. 4.7 Frequency responses and modal patterns obtained by (4.9) for the cavity shown in Fig. 4.3 with (a) $m=1, n=0$ (b) $m=0, n=1$, and (c) $m=1, n=1$, respectively.

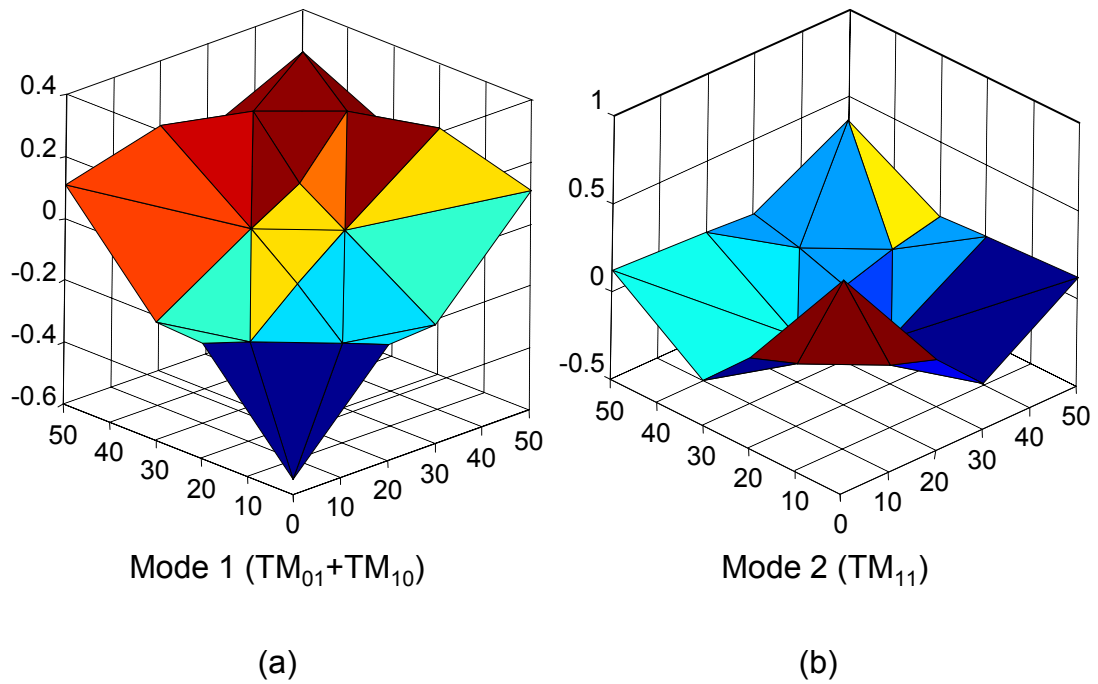


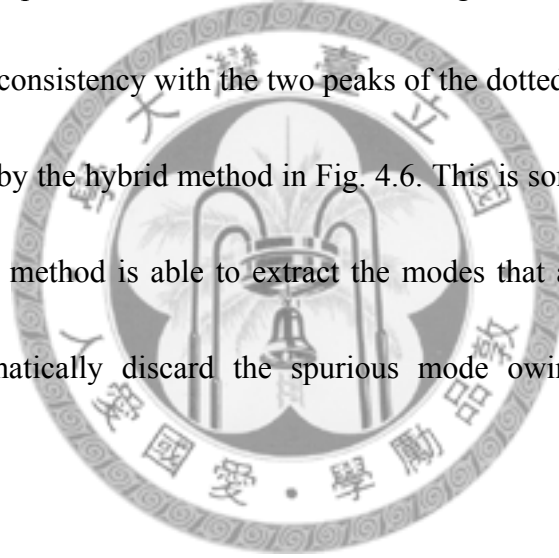
Fig. 4.8. Modal patterns of (a) the first mode and (b) the second mode extracted by the hybrid method for the structure shown in Fig. 4.3 with mesh settings shown in Fig. 4.4.

with some initial voltage $V_{0,mn}$ and phase ϕ_{mn} .

Fig. 4.7 shows the frequency responses and the modal patterns of the first three modes with lowest resonant frequencies obtained by (4.9) for the square cavity shown in Fig. 4.3. Comparing with the modal patterns of the first two modes

extracted by the hybrid method, which are shown in Fig. 4.8, the modal pattern of the first mode extracted by the hybrid method is exactly the linear combination of the first two degenerated modes TM_{10} and TM_{01} calculated by (4.9). The second mode extracted by the hybrid method can also be identified as TM_{11} mode, with a different phase from Fig. 4.7c.

The frequency responses of the modes shown in Fig. 4.7, which are calculated by (4.9), also show a consistency with the two peaks of the dotted line at the resonant frequencies obtained by the hybrid method in Fig. 4.6. This is somewhat a surprising result that the hybrid method is able to extract the modes that actually exist in the structures and automatically discard the spurious mode owing to coarse mesh settings.



4.3 A More Realistic Power-Ground Plane

4.3.1 Geometry

Fig. 4.9 shows a more realistic power-ground plane compare to the one in the previous section. The geometric parameters are shown in Fig. 4.9a where the top-right corner of a square metal plate with $w = l = 50\text{mm}$ is cut from $(35, 50)$ to

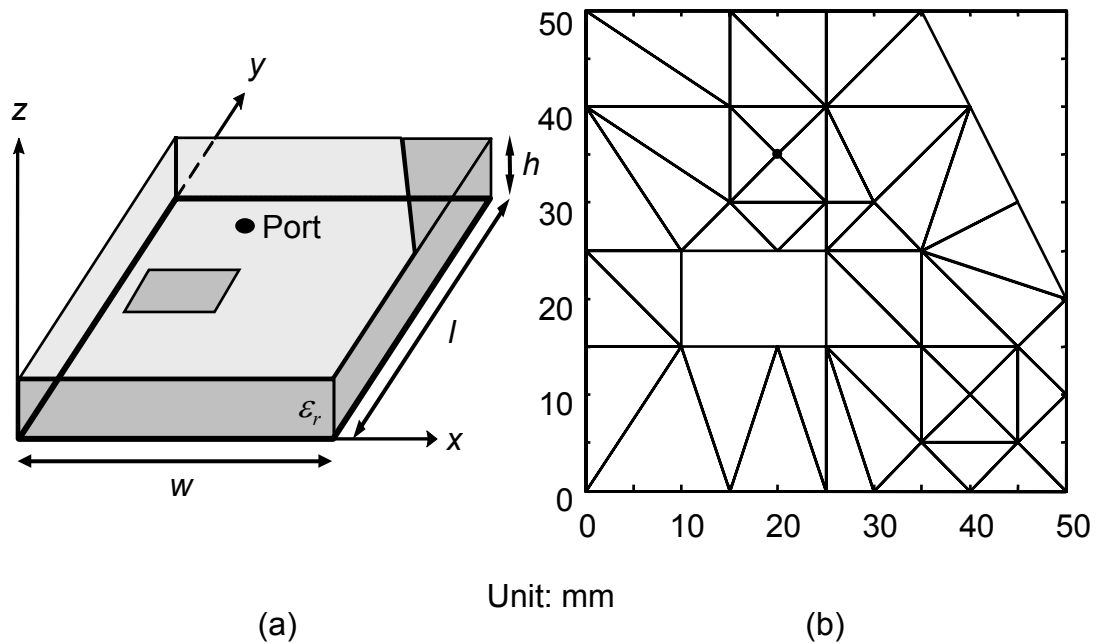


Fig. 4.9. A more realistic power-ground plane with a clipped corner and an aperture on the top metal. (a) The geometric parameters of the power-ground plane. (b) The mesh setting for simulation.

(50, 20). An aperture with a width 15mm and a height 10mm is also located on the same plate with its center at (17.5, 20). The power-ground planes are separated by a dielectric slab with a relative dielectric constant $\epsilon_r = 4.2$ and a height $h = 1.6$ mm.

Two different sources with their responses shown in Fig. 4.10 are injected to the port with coordinate (20, 35). Fig. 4.10a and Fig. 4.10b shows the time and frequency

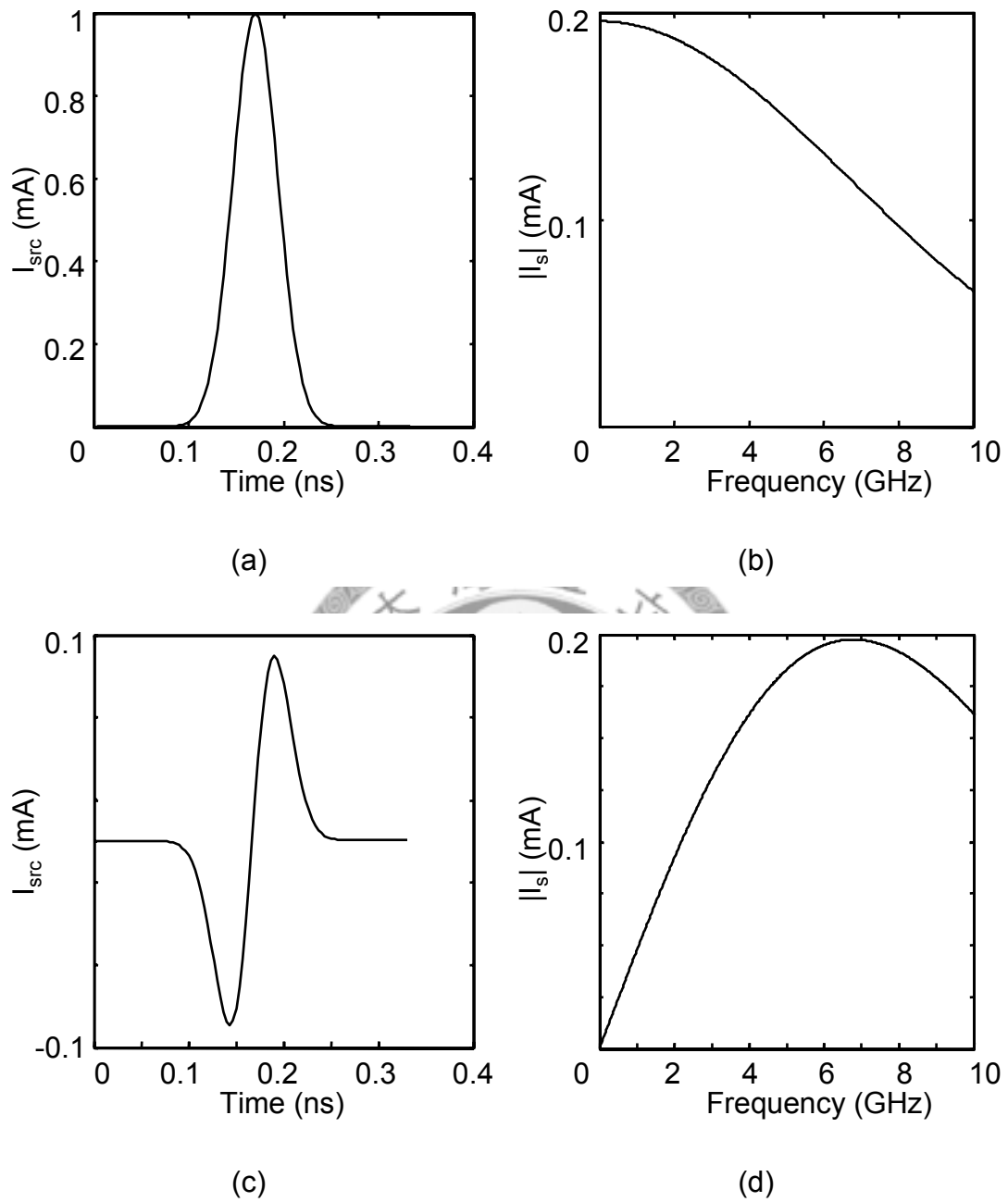


Fig. 4.10. (a) The time response of a standard Gaussian pulse and (b) its frequency response; and (c) the time response of a modulated Gaussian pulse with zero DC level and (d) its frequency response.

responses of the first current source with a standard Gaussian pulse response $I_s = I_0 \exp\left(-\frac{(t-t_0)^2}{t_d^2}\right)$, where $I_0 = 1\text{mA}$, $t_0 = 167\text{ps}$, and $t_d = 33\text{ps}$. This source is modulated by a 1GHz sine wave for the second source with a zero DC level, which has the time and frequency responses as shown in Fig. 4.10c and Fig. 4.10d, respectively. The input impedance at the same port is then calculated by frequency transforming the time responses of the voltage and current with FFT.

4.3.2 Simulation Results

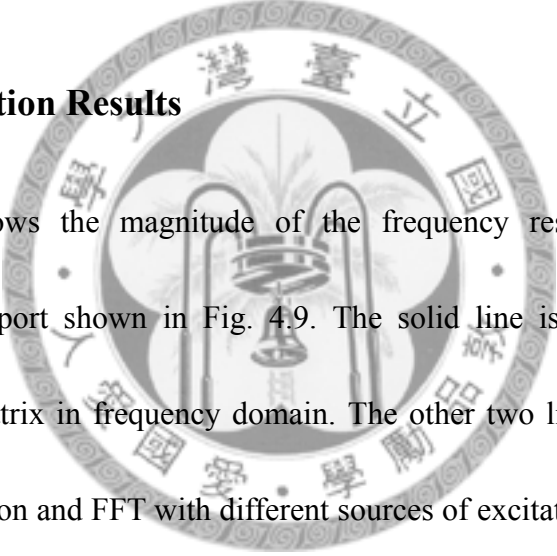


Fig. 4.11 shows the magnitude of the frequency responses of the input impedance at the port shown in Fig. 4.9. The solid line is obtained by directly inverting the Y-matrix in frequency domain. The other two lines are the results by time-domain iteration and FFT with different sources of excitation. The result plotted in dashed line is excited by the first source, in which a DC level at steady-state in time-domain is transformed into a delta response at zero frequency. Since most energy is confined at DC, the precision of the results obtained at other frequencies is limited. The result of the second excitation, a modulated Gaussian current pulse with zero DC level, is plotted in a dash-dotted line. The sharp transition at zero frequency no longer exists and responses at other frequencies become closer to the solid line.

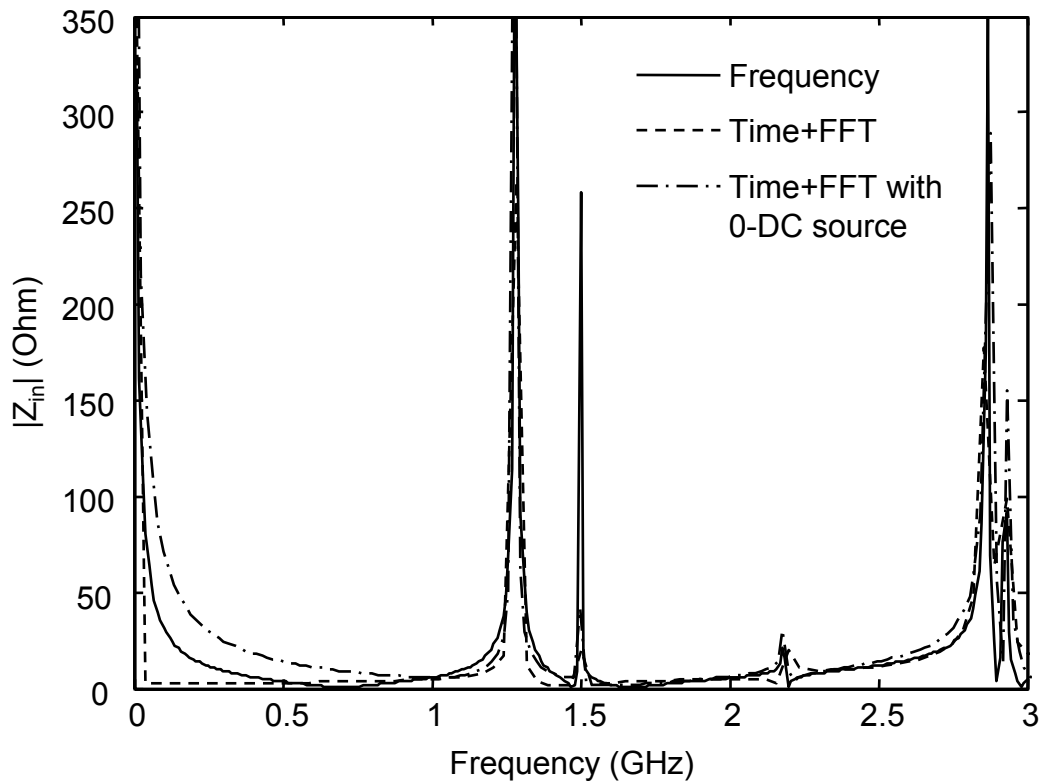


Fig. 4.11. The magnitude of the frequency responses of the input impedance at the port shown in Fig. 4.9. The solid line is obtained by direct inverting the Y-matrix in frequency domain. The dashed and dash-dotted lines are the results by time-domain iteration and FFT with two different sources of excitation.

The result of the hybrid method is also obtained and compared. Fig. 4.12 shows the magnitude of the frequency responses of the input impedance at the port shown in Fig. 4.9 obtained by direct time-domain iteration (solid line) and the hybrid method (dashed line) with FFT. As shown in the figure, the hybrid method is able to

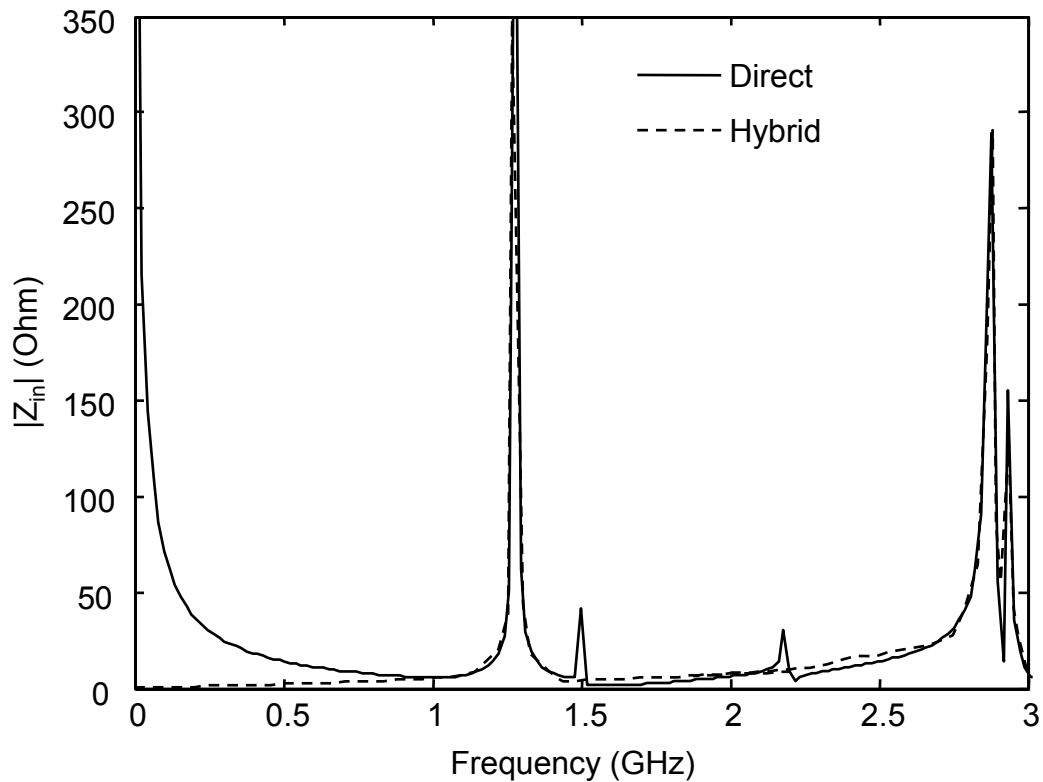


Fig. 4.12. The magnitude of the frequency responses of the input impedance at the port shown in Fig. 4.9 obtained by direct time-domain iteration (solid line) and the hybrid method (dashed line) with FFT.

extract the major resonant frequencies of the structure. However the two responses are quite different at low frequencies. This is due to the nature of the model-order reduction process in the hybrid method in which the resonant modes were extracted for the reconstruction of late-time responses. Since the pole at DC cannot be treated as a “resonant mode”, it cannot be extracted by the hybrid method.

4.3.3 Modal Patterns

The modal patterns of the first two modes extracted by the hybrid method are shown in Fig. 4.13a and Fig. 4.13b. The first mode, as shown in Fig. 4.13a, is basically a variation of the first mode extracted from the structure with no defected metal plate shown in Fig. 4.3 by the same method. However the combination of the two degenerated modes no longer exists since symmetry is destroyed by the cut corner. The second mode extracted in this case shows a quite different pattern as the one extracted from the structure shown in Fig. 4.3, because the symmetry for this mode is heavily destroyed by both the cut corner and the aperture.

The modal patterns for the same structures are also extracted by Ansoft[®] HFSS[™], a popular commercial full-wave simulation software package, for verification. The resulting modal patterns of same modes as Fig. 4.13a and Fig. 4.13b are shown in Fig. 4.13c and Fig. 4.13d, respectively, in which the magnitude and direction of electric field in the structure at different points are represented by the length and direction of arrows, respectively. It is obvious that the modal patterns for the first two modes extracted by the hybrid method are in good coherence to those extracted by HFSS. For example, for the first mode, both Fig. 4.13a and Fig. 4.13c

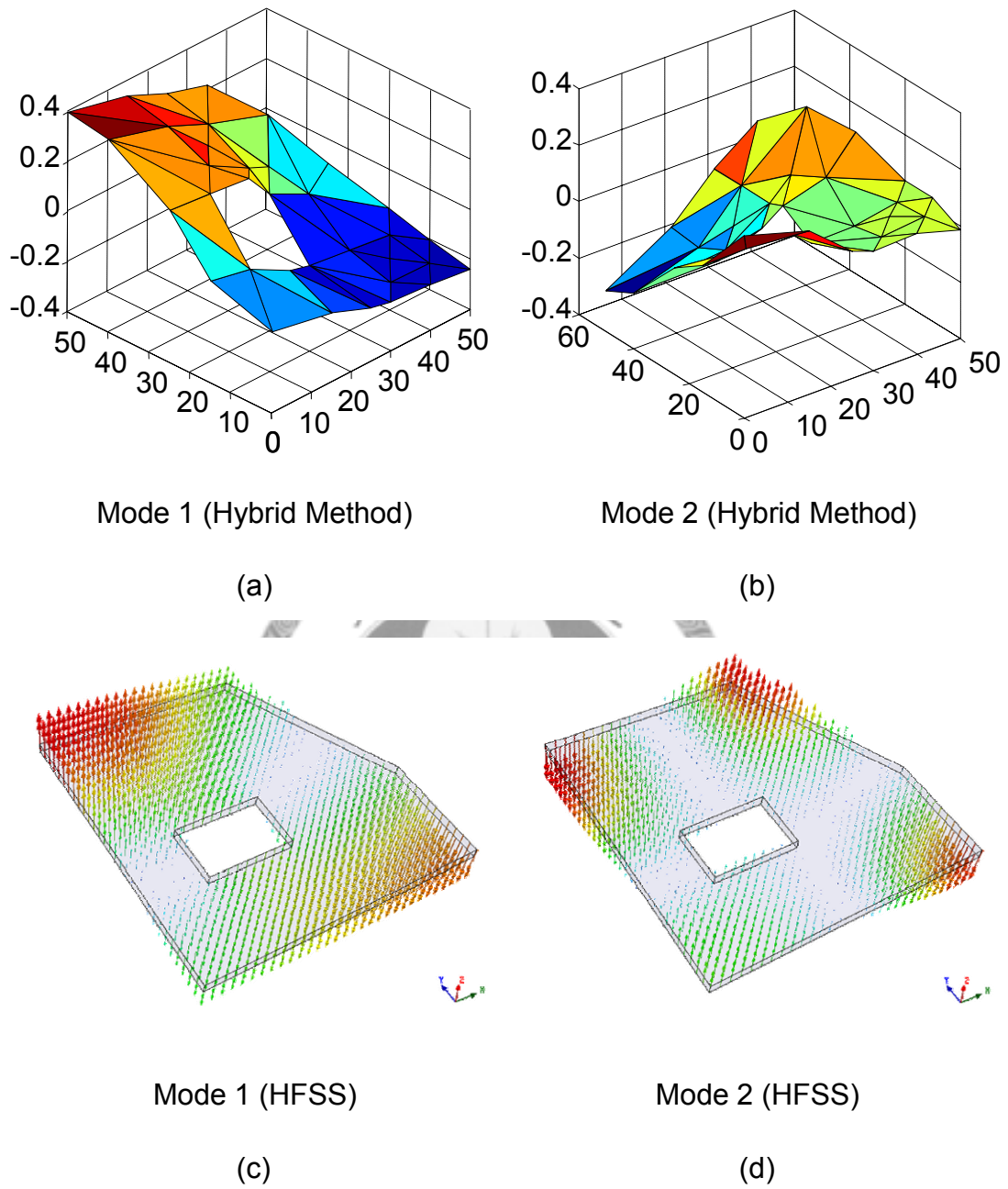


Fig. 4.13. (a) The first mode and (b) the second mode of the structure shown in Fig. 4.9, which are extracted by the hybrid method; and (c) the first mode and (b) the second mode of the same structure extracted by Ansoft[®] HFSS[™].

show that the strongest field occurs at the two corners next to the one cut, with opposite directions. The field decrease gradually along the diagonal connecting these two corner and zeroes occur along a line connecting the cut corner and the aperture.

4.4 Convergence and Complexity

The hybrid method proposed in this chapter is composed of three major parts, the Delaunay-Vononoi Modeling of Power-Ground Planes, the time-domain iteration, and model order reduction by Krylov subspace method. The convergence with respect to the three parts will be discussed separately. A self convergence test will also be given. The complexity analysis is based on the step-by-step algorithm provided in 4.1. Both the complexity of computation and memory overhead will be considered.

4.4.1 Convergence

The convergence analysis begins with the Delaunay-Vononoi modeling of power-ground planes, where the mesh arrangement reveals that the accuracy is associated with the longest distance between any two connected virtual or source ports. As for the probing frequencies, its accuracy is ranged from 0.20 to 0.25 of

wavelength interested [22].

Taking the simulation in 4.2 for example, the longest distance between the ports is $20\sqrt{2}$ mm, which means the highest frequency of accuracy results is ranged from 2GHz to 2.5GHz, according to the simulation parameters for this case. Inaccurate results such as spurious modes may arise above this frequency range, which can be observed in the simulation results.

As mentioned in [22], the domain of Delaunay-Voronoi modeling of power-ground planes reduced identically to the rectangular FDTD grid when the Voronoi tessellation becomes rectangular shape. Since the time-domain iteration based on this model, which is discussed in 4.1, is also updated with explicit equations in the same manner as FDTD, therefore the stability constraint in the Courant number

$$S = \frac{c\Delta t}{\Delta} \leq 1, \quad (4.10)$$

must be satisfied, where Δ is the smallest distance crossing a cell from one grid point to another [2].

As described in step 5) in the step-by-step implementation that summarized 4.1, in order to determine the number of modes that are needed to be extracted precisely,

the expansion coefficients of the eigenmodes are compared. After the Krylov subspace of order m is constructed, an approximate eigensolution set of the original system can be found by (2.20). The expansion coefficient a_i associated with θ_i is calculated by taking the inner product with the voltage vectors \mathbf{V}^{n_0} at the n_0 -th time step of FDTD iteration that the Lanczos algorithm starts. Terms with small expansion coefficient can then be dropped safely.

In order to verify the self convergence of the hybrid method proposed in this chapter, a set of three mesh settings from coarser to finer for the structure shown in Fig. 4.3 is arranged as shown in Fig. 4.14. The space division in both x and y directions are 10mm, 5mm, and 10/3mm for Mesh1 in Fig. 4.14a, Mesh2 in Fig. 4.14b, and Mesh3 in Fig. 4.14c, respectively. A Gaussian current pulse $I_s = I_0 \exp\left(-\frac{(t-t_0)^2}{t_d^2}\right)$, with $I_0 = 1\text{mA}$, $t_0 = 10\text{ns}$, and $t_d = 2\text{ns}$ is injected to excite the structure.

The frequency responses of the input impedances at the incident port denoted by black dots in Fig 4.13 for all three mesh settings are calculated by frequency transforming the late-time response obtained by the hybrid methods with FFT. Results are plotted in Fig. 4.15, where the dotted, dashed, and solid lines are obtained

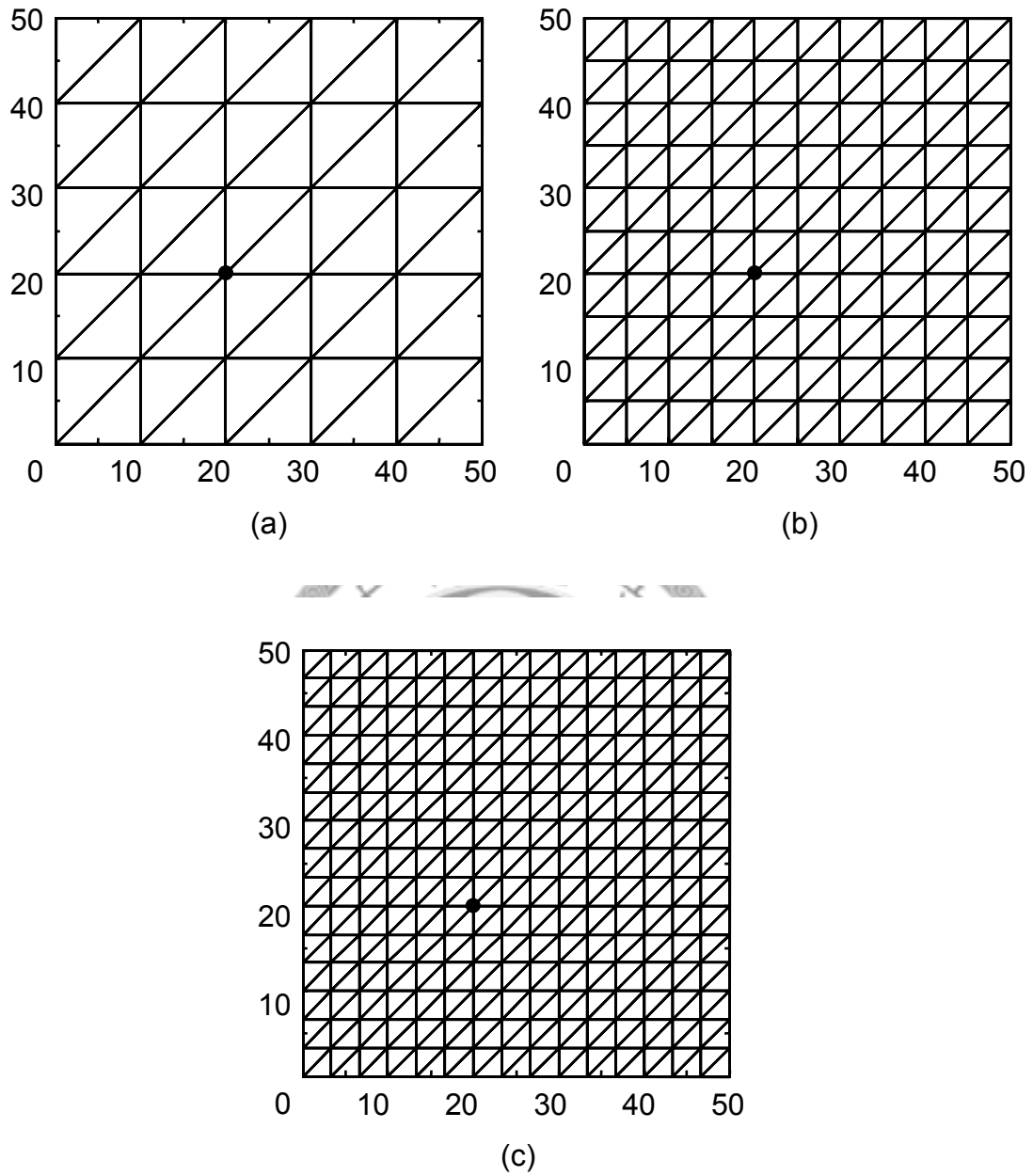


Fig. 4.14. (a) Mesh1, a coarse mesh setting, (b) Mesh2, a marginal mesh setting, and (c) Mesh3, a fine mesh setting arranged for the verification of self convergence of the hybrid method proposed in this chapter.

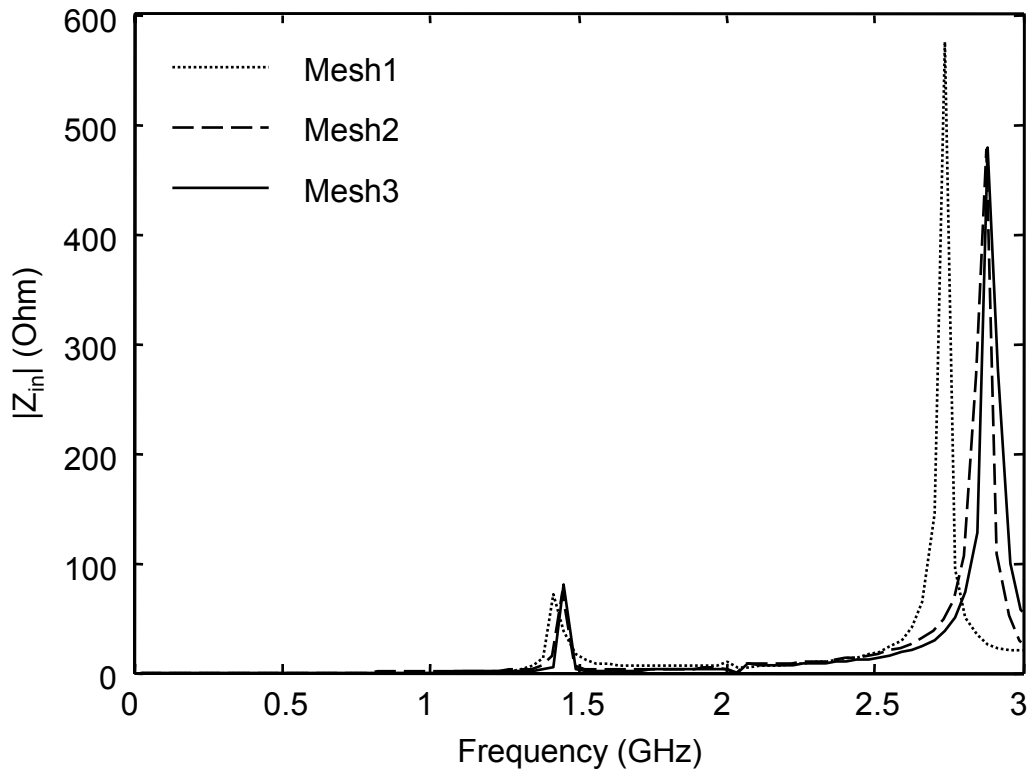


Fig. 4.15. Frequency responses of the input impedances at the incident port denoted by black dots in Fig 4.13 for mesh settings Mesh1 (dotted line), Mesh 2 (dashed line), and Mesh3 (solid line).

with mesh settings Mesh1, Mesh2, and Mesh3, respectively. It is obvious that as the mesh settings become finer, both resonant frequencies obtained converge to fixed values.

Modal patterns are also extracted. Fig. 4.16 shows the modal patterns of the first

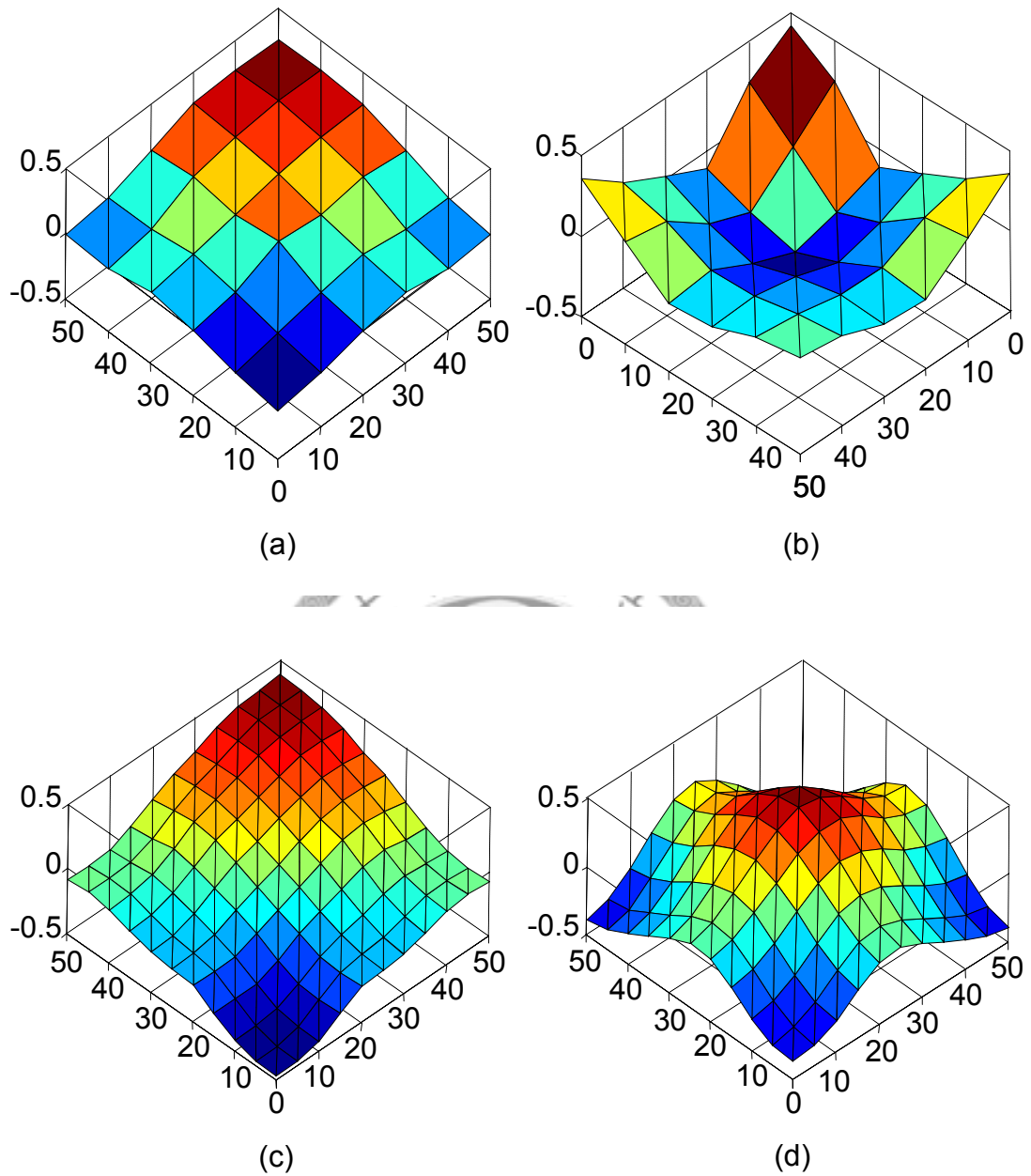


Fig. 4.16. Modal patterns extracted by the hybrid method. (a) The first mode and (b) the second mode extracted from Mesh1; and (c) The first mode and (d) the second mode extracted from Mesh2.

two modes extracted by the hybrid method for mesh settings Mesh1 and Mesh2. Fig. 4.16a and Fig. 4.16c shows the modal patterns of the first mode extracted from Mesh1 and Mesh2, respectively. It is obvious that these two patterns are identical. The second modal patterns extracted from Mesh1 (Fig. 4.16b) and Mesh2 (Fig. 4.16d) can also be recognized as the same pattern except for an inverted phase.

4.4.2 Complexity

As discussed in 3.4.2, a frequency response with a higher resolution in frequency requires a longer time period of steady-state response in time-domain. The previous subsection also mentioned that for the hybrid method proposed in this chapter to converge, a finer mesh setting in space leads to a smaller division in time as traditional FDTD simulation does. As a result, more simulation time is needed for better frequency resolution.

Assume that a mesh setting for some structure is determined for simulation by the hybrid method. According to the step-by-step algorithm that concludes 4.1, an equivalent circuit network for a structure is firstly constructed using Delaunay-Voronoi modeling. If a network of total number P nodes and branches is constructed,

$O(P)$ basic arithmetic operations, e.g., multiplications and accumulations, is required for computing the values of capacitors and inductors.

After constructing the equivalent circuit network, a total number P of voltage and current values is required to be updated in every time step for the time-domain iteration. If L time steps are taken for the sources to fade to zero and the modal patterns begin to appear and after that N time steps are performed for a satisfactory frequency resolution. The overall computation time for the time-domain iteration is linearly proportional to the number of field points and total time step computed, or $O(P \cdot (L + N))$.

For the proposed hybrid method, normal time-domain iteration is firstly applied for the same L time steps. Krylov subspace method is then constructed for model-order reduction. Assume that a necessary number of voltage vectors are stored for the model order reduction process to converge without penalty and Q modes need to be extracted precisely and the Lanczos algorithm converges at the M -th time step. For constructing a one-order-larger Krylov subspace, at most Q modal expansion coefficients are obtained and the eigensolution of the $m \times m$ tridiagonal matrix is also solved for the convergence criteria.

After that, the frequency response at a single field point with the same resolution can be directly obtained in $O(N)$ basic arithmetic operations. The overall complexity of the hybrid method is therefore $O(P \cdot L + Q \cdot N + M^2)$. In the usual cases, $Q \leq M \ll L \ll N \ll P$, thus the normal time-domain iteration has an $O(P \cdot N)$ complexity, whereas the hybrid method reduces the complexity to $O(P \cdot L)$.

When penalty occurs, however, the overall model order reduction process is repeated with a larger number of voltage vectors. This means that another $O(M^2)$ operation is required for the new model order reduction process to complete. Although an $O(M^2)$ operation is a small part of the overall hybrid method, doing the same operation repeatedly with only another starting value is still a time-wasting job if penalty occurs too often.

Penalty can be avoided by pre-storing a larger number of voltage vectors for the construction of Krylov subspace. If plenty of voltage vectors are pre-stored, penalty never occurs. It is obvious that every vector pre-stored requires an $O(P)$ of memory spaces and a minimum memory space of $O(M \cdot P)$ is required for the model order reduction process to converge without penalty. Since this minimum size of memory

space is unknown before completing the model order reduction process, overestimating the number of voltage vectors is necessary. If this number is chosen too large such that secondary storage is used, the overall performance will be seriously reduced by the model order reduction process.

4.5 Summary of the Chapter

A hybrid method combining the Delaunay-Voronoi modeling of power-ground planes in time-domain and Krylov subspace method is proposed in this chapter. Taking advantage of the space information, only few time-domain iterations before the sources fade to zero is required for extracting the excited modes and reconstructing the late time response by analytic expression. With a simple example and a more realistic case, the correctness, efficiency, convergence, and complexity of this method have been verified.



5

Conclusions

HYBRID methods that able to construct the late-time response of a system have been proposed in this thesis. In general, Krylov subspace method based model order reduction technique is applied to time domain full-wave electromagnetic simulations after the sources fade to zero for extracting the active modes in the system. Late-time responses are then constructed by the linear combination of the extracted modes.

This chapter concludes the thesis by firstly provide a summary of the work, where the basic concept and typical application of the hybrid methods proposed in this thesis will be briefly reviewed. Several suggestions for the future work, according to the limitations and disadvantages in the present development of the proposed hybrid methods, will then be given for those interested in the further study of these methods.

5.1 Summary of the Work

Two different hybrid methods based on the same concept are presented in this thesis. Beginning from the theories developed in chapter 2, the first hybrid method constructs the late-time response by combining finite-difference time-domain method and Lanczos algorithm, whereas the second hybrid method constructs Krylov subspaces directly for the approximation of Delaunay-Voronoi modeling of power-ground planes in time-domain. Taking advantage of the space information, both methods requires only few direct time domain iterations before the sources fade to zero with additional round-trip time before the extraction of the excited modes. After the dominant modes are properly extracted, the late time response of the system can be easily reconstructed by analytic expressions.

The hybrid method combining FDTD and Lanczos algorithm proposed in chapter 3 is able to reconstruct the late-time response of the large systems efficiently and faithfully. Results of the hybrid method such as late-time responses, frequency responses, and modal patterns have been calculated and compared to those obtained from direct FDTD iterations. The correctness, efficiency, convergence, and complexity have been verified for the closed systems in the demonstration cases.

Existing FDTD codes are preserved by introducing the time-reversal technique in the FDTD iterations. Although suitable for problems with non-magnetic material only, the hybrid method still applies in common problems.

The hybrid method combining the Delaunay-Voronoi modeling of power-ground planes in time-domain and Krylov subspace method proposed in chapter 4 is also suitable for efficient and faithful reconstruction of late-time responses. Both a simple example and a more realistic case are provided for demonstration. Results such as the late-time responses, frequency responses obtained by the hybrid method and direct time domain iteration are in good agreements. Modal patterns are also highly coherent to the results from the popular commercial full-wave electromagnetic simulation software package, Ansoft® HFSS™.

5.2 Suggestions for Future Work

Further studies of the hybrid methods proposed in this work are suggested in two aspects. One is extending the range of applications, such as systems with not only non-magnetic materials, systems with lossy dielectrics, or high-Q materials in systems with open boundaries. The other is to enhancing the performance, for

example, faster convergence or less memory requirement in the model order reduction process.

Extending the range of applications can be accomplished by introducing the Krylov subspace methods for non-symmetric systems in the model order reduction process, in the mean time complex eigenpairs will also be generated for the approximation of both the attenuation constants and wave numbers of resonant modes, symmetric systems, systems with lossy media, or high-Q materials in systems with open boundaries will then be applicable. In order to integrate the Krylov subspace methods for non-symmetric systems into the hybrid method, however, modification of existing time-domain simulation code will be necessary because both the original and its adjoint problems are required. Convergence problems will also arise with Krylov subspace methods for non-symmetric systems [15]. Therefore minimizing the modification of existing to assure code reuse and avoiding the convergence issues with asymmetric Krylov subspace methods will be the primary challenges in extending the application range of the hybrid method.

The performance of the hybrid method may be enhanced by applying the model order reduction process to smaller vectors containing a smaller subset of field values

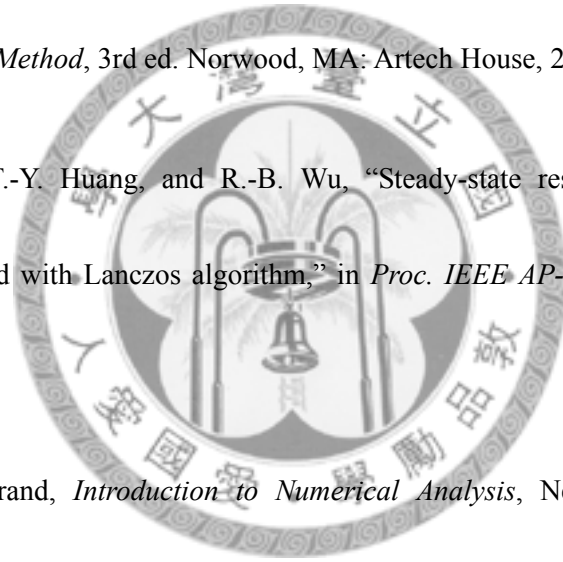
in the solution space of the systems. The Krylov subspace can then be constructed faster and vectors that are necessary for the construction of Krylov subspace can also be stored with less memory requirement. However, less space information may result in longer converging time since more time information is needed to compensate the missing space information. Tradeoffs between space and time information for the eigenmodes of systems may become a major problem for enhancing the performance of the hybrid methods.





References

- [1] K. S. Yee, "Numerical solution of initial boundary value problems involving Maxwell's equations in isotropic media," *IEEE Trans. Antennas Propag.*, vol. AP-14, no. 5, pp. 302–307, May 1966.
- [2] A. Taflove and S. C. Hagness, *Computational Electrodynamics: The Finite-Difference Time-Domain Method*, 3rd ed. Norwood, MA: Artech House, 2005.
- [3] Y.-H. Pang, T.-Y. Huang, and R.-B. Wu, "Steady-state response by time-reversal FD-TD method with Lanczos algorithm," in *Proc. IEEE AP-S*, Jun. 2003, vol. 4, pp. 356–359.
- [4] F. B. Hilderbrand, *Introduction to Numerical Analysis*, New York: Dover, 1974, pp.457-462.
- [5] J. L. Dubard, P. Pompei, J. Le Roux, and A. Papiernic, "Characterization of microstrip antennas using the TLM simulation associated with a Prony-Pisrenko method," *Intl. J. Numerical Modeling*, Vol. 3. pp. 269-285, Mar. 1990.
- [6] W. L. Ko and R. Mittra, "A combination of FD-TD and Prony's methods for analyzing microwave integrated circuits," *IEEE Trans. Microw. Theory Tech.*, vol. 39, no. 12, pp.



- 2176–2181, Dec. 1991.
- [7] J. A. Pereda, L. A. Vielva, and A. Prieto, “Computation of resonant frequencies and quality factors of open dielectric resonators by a combination of finite-difference time-domain (FDTD) and Prony’s methods,” *IEEE Microw. Guided Wave Lett.*, vol. 2, pp. 431-433, Feb. 1992.
- [8] K. Naishadham and X. P. Lin, “Application of spectral domain Prony’s method to the FDTD analysis of planar microstrip circuits,” *IEEE Trans. Microw. Theory Tech.*, vol. 42, no. 12, pp. 2391–2398, Dec. 1994.
- [9] M. R. Wall and D. Neuhauser, “Extraction, through filter-diagonalization of general quantum eigenvalues or classical normal-mode frequencies from a small number of residues or a short-time segment of a signal: 1. Theory and application to a quantum-dynamics model,” *J. Chem. Phys.*, vol. 102, pp. 8011-8022, 1995.
- [10] R. Q. Chen and H. Guo, “Efficient calculation of matrix elements in low storage filter diagonalization,” *J. Chem. Phys.*, vol. 111, pp. 464-471, 1999.
- [11] S. G. Johnson, S. Fan, A. Mekis, and J. D. Joannopoulos, “Multiple-cancellation mechanism for high-Q cavities in the absence of a complete photonic band gap,”

- Applied Phys. Lett.*, vol. 78, pp. 3388-3390, 2001.
- [12] S. G. Johnson, A. Mekis, S. Fan, and J. D. Joannopoulos, "Molding the flow of light," *IEEE Comput. Sci. Eng. Mag.*, vol. 3, pp. 38-47, Nov./Dec. 2001.
- [13] V. A. Mandelshtam and H. S. Taylor, "Harmonic inversion of time signals and its applications," *J. Chem. Phys.*, vol. 107, pp. 6756-6769, Nov. 1997.
- [14] S. Pissanetzky, *Sparse Matrix Technology*. London, U.K.: Academic, 1984, sec. 6.11.
- [15] G. H. Golub and C. F. Van Loan, *Matrix Computations*, 3rd ed. London, U.K.: The Johns Hopkins Univ. Press, 1996, ch. 9.
- [16] R. F. Remis and P. M. van den Berg, "A modified Lanczos algorithm for the computation of transient electromagnetic wavefields," *IEEE Trans. Microw. Theory Tech.*, vol. 45, no. 12, pp. 2139-3149, Dec. 1997.
- [17] A. C. Cangellaris and L. Zhao, "Rapid FDTD simulation without time stepping," *IEEE Microw. Guided Wave Lett.*, vol. 9, no. 1, pp. 4-6, Jan. 1999.
- [18] Y. Saad, "The Lanczos biorthogonalization algorithm and other oblique projection methods for solving large unsymmetric systems," *SIAM J. Numer. Anal.*, vol. 19, no. 3, pp. 485-506, Jan. 1982.

- [19] T.-Y. Huang and R.-B. Wu, "Steady-state response by finite-difference time-domain method and Lanczos algorithm," *IEEE Trans. Microw. Theory Tech.*, Vol. 54, No. 7, pp. 3038-3044, Jul. 2006.
- [20] R. Sorrentino, L. Roselli, and P. Mezzanotte, "Time reversal in finite difference time domain method," *IEEE Microw. Guided Wave Lett.*, vol. 3, no. 11, pp. 402–404, Nov. 1993.
- [21] K.-B. Wu, G.-H. Shiue, W.-D. Guo, and R.-B. Wu, "An efficient and flexible modeling for power/ground planes," *Proc. 2006 Electrical Performance of Electronic Packaging*, pp. 83-86, Oct. 2006.
- [22] K.-B. Wu, G.-H. Shiue, W.-D. Guo, C.-M. Lin, and R.-B. Wu, "Delaunay–Voronoi modeling of power-ground planes with source port correction," *IEEE Trans. Adv. Packaging*, vol. 32, no. 2, May 2008.
- [23] R.-B. Wu and T. Itoh, "Hybrid finite-difference time-domain modeling of curved surfaces using tetrahedral edge elements," *IEEE Trans. Antennas Propag.*, vol. 45, no. 8, pp. 1302–1309, Aug. 1997.
- [24] D. M. Pozar, *Microwave Engineering*, 2nd Ed., New York, US: John Wiley & Sons,

Inc., New York, 1998, Ch. 6.





Publication List of Ting-Yi Huang

A. Journal Papers

- [1] C.-F. Chen, T.-Y. Huang, and R.-B. Wu, "A miniaturized net-type microstrip bandpass filter using $\lambda/8$ resonators," *IEEE Microw. Guided Wave Lett.*, Vol. 15, No. 7, pp. 481-483, Jul. 2005.
- [2] S.-H. Lee, T.-Y. Huang, and R.-B. Wu, "Fast waveguide eigenanalysis by wide-band finite-element model-order reduction," *IEEE Trans. Microw. Theory Tech.*, Vol. 53, No. 8, pp. 2552-2558, Aug. 2005.
- [3] C.-F. Chen, T.-Y. Huang, C.-H. Tseng, R.-B. Wu, and T.-W. Chen, "A miniaturized multilayer quasi-elliptic bandpass filter with aperture-coupled microstrip resonators," *IEEE Trans. Microw. Theory Tech.*, Vol. 53, No. 9, pp. 2688-2692, Sep. 2005.
- [4] C.-F. Chen, T.-Y. Huang, and R.-B. Wu, "Design of microstrip bandpass filters with multiorder spurious-mode suppression," *IEEE Trans. Microw. Theory Tech.*, Vol. 53, No. 12, pp. 3788-3793, Dec. 2005.
- [5] C.-F. Chen, T.-Y. Huang, and R.-B. Wu, "Novel compact net-type resonators and their

- applications to microstrip bandpass filters,” *IEEE Trans. Microw. Theory Tech.*, Vol. 54, No. 2, pp. 755-762, Feb. 2006.
- [6] C.-F. Chen, T.-Y. Huang, C.-P. Chou, and R.-B. Wu, “Microstrip diplexers design with common resonator sections for compact size, but high isolation,” *IEEE Trans. Microw. Theory Tech.*, Vol. 54, No. 5, pp. 1945-1952, May. 2006.
- [7] T.-Y. Huang and R.-B. Wu, “Steady-state response by finite-difference time-domain method and Lanczos algorithm,” *IEEE Trans. Microw. Theory Tech.*, Vol. 54, No. 7, pp. 3038-3044, Jul. 2006.
- [8] C.-F. Chen, T.-Y. Huang, and R.-B. Wu, “Design of dual- and triple-passband filters using alternately cascaded multiband resonators,” *IEEE Trans. Microw. Theory Tech.*, Vol. 54, No. 9, pp. 3550-3558, Sep. 2006.
- [9] T.-M. Shen, C.-F. Chen, T.-Y. Huang, and R.-B. Wu, “Design of vertically stacked waveguide filters in LTCC,” *IEEE Trans. Microw. Theory Tech.*, Vol. 55, No. 8, pp. 1771-1779, Aug. 2007.
- [10] A.-S. Liu, T.-Y. Huang, and R.-B. Wu, “A dual wide-band filter design using frequency mapping and stepped-impedance resonators,” submitted to *IEEE Trans. Microw.*

Theory Tech.

B. Conference Papers

- [1] T. Y. Huang, Y. H. Pang, and R. B. Wu, "Full-wave optimization by EM3D technology and genetic algorithm," *2002 Asia-Pacific Microwave Conference Proceedings*, pp.307-308, Kyoto, Japan, Nov. 2002.
- [2] Y. H. Pang, T. Y. Huang, and R. B. Wu, "Steady-state response by time-reversal FD-TD method with Lanczos algorithm," *2003 IEEE AP-S International Symposium on Antennas and Propagation*, pp.356-359, Columbus, OH, USA, Jun. 2003
- [3] T.-H. Yang, C.-F. Chen, T.-Y. Huang, C.-L. Wang, and R.-B. Wu, "A 60GHz LTCC transition between microstrip line and substrate integrated waveguide," *2005 Asia-Pacific Microwave Conference Proceedings*, pp. 469-471, China, Dec. 2005
- [4] C.-F. Chen, T.-Y. Huang, and R.-B. Wu, "Compact microstrip cross-coupled bandpass filters using miniaturized stepped impedance resonators," *2005 Asia-Pacific Microwave Conference Proceedings*, pp. 493-496, China, December 2005.
- [5] T.-M. Shen, T.-Y. Huang, C.-F. Chen, and R.-B. Wu, "Design of 60GHz vertically

- stacked waveguide filters in LTCC,” *2005 Asia-Pacific Microwave Conference Proceedings*, pp. 733-735, China, Dec. 2005.
- [6] T.-Y. Huang, Y.-C. Yu, and R.-B. Wu, “Dual-band/broadband circular polarizers designed with cascaded dielectric septum loadings,” *Progress in Electromagnetics Research Symposium Proceedings*, pp. 475-477, Cambridge, MA, USA, Mar. 2006.
- [7] C.-F. Chen, T.-Y. Huang, and R.-B. Wu, “Miniaturized microstrip quasi-elliptical bandpass filters using slotted resonators,” *2006 IEEE International Microwave Symposium*, pp. 1185-1188, San Francisco, CA, USA, Jun. 2006.
- [8] T.-M. Shen, T.-Y. Hung, C.-F. Chen, and R.-B. Wu, “Design of a Vertically stacked waveguide filter with novel cross coupling structures in LTCC,” *2006 Asia-Pacific Microwave Conference Proceedings*, Vol. 2, pp. 1161-1164, Japan, Dec. 2006.
- [9] C. F. Chen, T.-Y. Huang, and R.-B. Wu, “A miniaturized microstrip common resonator triplexer without extra matching network,” *2006 Asia-Pacific Microwave Conference Proceedings*, Vol. 3, pp. 1439-1442, Japan, Dec. 2006.
- [10] C. F. Chen, T. M. Shen, T. Y. Huang, and R. B. Wu, “Design of microstrip contiguous broadband diplexers for cosmic microwave background detection,” *URSI/SAS 2007*

- Radio Science Conference and Taiwan-Japan Joint Meeting on Antennas and Propagation*, Tao-Yuan, Taiwan, Mar. 2007.
- [11] C. K. Yau, T. Y. Huang, T. M. Shen, H. Y. Chien, and R. B. Wu, "Design of 30GHz transition between microstrip line and substrate integrated waveguide," *2007 Asia-Pacific Microwave Conference Proceedings*, pp. 243-246, Bangkok, Thailand, Dec. 2007.
- [12] T. M. Shen, T. Y. Lin, T. Y. Huang, and R. B. Wu, "A vertically stacked quasi-elliptic waveguide filter with crossly coupling vias," *2007 Asia-Pacific Microwave Conference Proceedings*, pp. 667-670, Bangkok, Thailand, Dec. 2007.
- [13] H. Y. Chien, T. M. Shen, T. Y. Huang, and R. B. Wu, "Design of a vertically stacked substrate integrated folded-waveguide resonator filter in LTCC," *2007 Asia-Pacific Microwave Conference Proceedings*, pp. 675-678, Bangkok, Thailand, Dec. 2007.
- [14] W. L. Chang, T. Y. Huang, T. M. Shen, B. C. Chen, and R. B. Wu, "Design of compact branch-line coupler with coupled resonators," *2007 Asia-Pacific Microwave Conference Proceedings*, pp. 1375-1378, Bangkok, Thailand, Dec. 2007.
- [15] B. C. Chen, T. M. Shen, T. Y. Huang, and R. B. Wu, "A dual pass band filter with

embedded CPW resonator,” *2007 Asia-Pacific Microwave Conference Proceedings*, pp.

1803-1806, Bangkok, Thailand, Dec. 2007.

